Zhao *et al. Chem Synth* 2024;4:41
**DOI:** 10.20517/cs.2024.42

**Chemical Synthesis**

**Review**

**Open Access**

# Hierarchical metal–organic framework nanoarchitectures for catalysis

**Bin Zhao[1], Ji Han[1], Bohan Liu[1], Song Lin Zhang[2], Buyuan Guan[1,3,*]**

[1]State Key Laboratory of Inorganic Synthesis and Preparative Chemistry, College of Chemistry, Jilin University, Changchun 130012, Jilin, China.
[2]Institute of Materials Research and Engineering (IMRE), Agency for Science, Technology and Research (A*STAR), Singapore 138634, Singapore.
[3]International Center of Future Science, Jilin University, Changchun 130012, Jilin, China.

[*]**Correspondence to:** Prof. Buyuan Guan, State Key Laboratory of Inorganic Synthesis and Preparative Chemistry, College of Chemistry, Jilin University, Qianjin Street 2699, Changchun 130012, Jilin, China. E-mail: guanbuyuan@jlu.edu.cn

**How to cite this article:** Zhao B, Han J, Liu B, Zhang SL, Guan B. Hierarchical metal–organic framework nanoarchitectures for catalysis. *Chem Synth* 2024;4:41. https://dx.doi.org/10.20517/cs.2024.42

**Received:** 31 Mar 2024 **First Decision:** 19 Apr 2024 **Revised:** 28 May 2024 **Accepted:** 4 Jun 2024 **Published:** 8 Jul 2024

**Academic Editor:** Guangshan Zhu **Copy Editor:** Pei-Yun Wang **Production Editor:** Pei-Yun Wang

## Abstract

Metal–organic frameworks (MOFs) have garnered significant attention in the field of catalysis due to their unique advantages such as diverse coordination geometry, variable metal nodes, and organic linkers, facilitating precise structural and compositional control for achieving programmable catalytic functionalities. Although their inherent microporous structure could provide excellent shape selectivity during catalysis, it typically impedes the mass transfer process, thereby reducing the use of internal active sites and overall catalytic efficiency. Additionally, employing single MOFs as catalysts presents challenges in achieving complex catalytic reactions that require multifunctional active sites. In recent years, considerable research efforts have focused on designing and constructing hierarchical nanostructured MOFs to alleviate substrate diffusion limitations by introducing secondary nanopores, shortening diffusion distances via the construction of low-dimensional nanoarchitectures, and constructing multifunctional catalysts by integrating distinct MOFs with suitable functions. This review provides a comprehensive overview of the design, synthesis methods, and formation mechanisms of MOF-based hierarchical nanostructures in recent years. Subsequently, it further highlights their applications in thermal catalysis, electrocatalysis, and photocatalysis, along with the relationship between their hierarchical nanostructures and catalytic performances. Finally, it provides an outlook on the challenges and potential development directions of hierarchically structured MOF nanocatalysts.

**Keywords:** Metal–organic frameworks, hierarchical nanoarchitectures, thermal catalysis, electrocatalysis, photocatalysis

## INTRODUCTION

As an important branch of porous crystalline materials, metal–organic frameworks (MOFs) are networks constructed from metal nodes coordinated to organic linkers[1,2]. Their unique pore structures give them distinct advantages in capturing, storing, and catalyzing guest ions and molecules, leading to widespread attention in fields such as catalysis, energy storage, sensing, and biomedicine[3]. The diverse pore structures and customizable chemical compositions of MOFs make them outstanding heterogeneous catalysts across a broad range of catalytic reactions[4-6]. Specifically, the tunable microporous structure not only offers exceptional size/shape selectivity but can also encapsulate guest species with various functions. Their ultra-large specific surface area could realize adsorption and enrichment of reaction substrates and provide abundant active sites for heterogeneous catalysis. Moreover, the diversity of functional metal ions/clusters and organic ligands could further broaden the applicability of MOFs to various potential catalytic systems, and organic-inorganic hybrid structures could exhibit unique synergies while maintaining their individual advantages[7-9]. Despite the advantages of MOFs for catalysis mentioned above, the inherent micropore structure of traditional MOFs hinders the mass transport of reactants within their pore systems, leading to the underutilization of active sites inside the MOF catalysts. Furthermore, the limited functions of single MOF materials present a significant challenge in achieving complex catalytic reactions that require multiple functional active sites[10,11].

One feasible approach to address the diffusion limitations or achieve multifunctional catalytic sites is rational design and synthesis of suitable MOF catalysts with increasingly complex hierarchical nanostructures[9,12-18]. Specifically, (i) introducing secondary meso-/macropores could increase the diffusion pathways of the reactants to mitigate diffusion limitation, provide necessary accessibility for large-size substrates, control the residence time of the reactants in the skeleton, and, thus, improve the catalytic reaction yield and selectivity[19-25]; (ii) Compared to traditional three-dimensional (3D) MOFs with large particle sizes, low-dimensional MOF nanostructures, such as nanoparticles, nanowires, and nanosheets, exhibit significantly increased surface-to-volume ratios. Such dimensional variance could effectively shorten the diffusion pathways for reactants through the microporous matrix, expose more accessible active sites, and increase the overall utilization efficiency of the MOF materials[26-32]; (iii) In addition to traditional synthesis routes leading to single MOF materials, integrating MOFs containing different desirable functions into heterostructures could significantly enrich the nanostructures and functionalities of the resultant MOF composite catalysts, expand the application range of catalysts, and realize complex catalytic reactions such as sequential and enzyme-mimicking catalysis[10,33-36]. Therefore, researchers aim to gain better control over the assembly and growth processes, allowing for the synthesis of MOF catalysts with unique hierarchical architectures and enhanced properties for specific catalytic applications[17,37-43].

In recent years, the study of hierarchical MOF nanoarchitectures has grown by leaps and bounds, and various novel and ingenious methods have been used to construct complex nanostructures of hierarchical MOFs. Therefore, to provide systematic and comprehensive guidance for synthesizing hierarchical nanostructures of MOFs themselves, we systematically examine the principles of various novel synthesis strategies in recent years from a more understandable perspective and provide a clearer insight into their structure-performance relationship. This review summarizes and analyzes the recent research progress on the synthesis methods and formation mechanisms of hierarchical MOF nanostructures. Subsequently, we discuss their applications and structure-performance relationships in thermal catalysis, electrocatalysis, and photocatalysis. Finally, we provide an outlook on the challenges and future directions in designing and synthesizing complex nanostructured catalysts of hierarchical MOFs.

## STRATEGIES FOR PREPARING MOFS WITH HIERARCHICAL NANOARCHITECTURES

So far, various ingenious methods have been used to construct hierarchical MOF nanoarchitectures. Based on their formation processes, synthesis techniques can be categorized into bottom-up and top-down routes [Table 1, Figure 1]. Bottom-up approaches involve cooperative assembly of MOF precursors with surfactant soft templates[44], growth under confinement using hard templates[45], and epitaxial growth of one MOF on the other caused by lattice matching[10]. On the contrary, top-down methods involve the delicate construction of MOF precursors, followed by generating new MOF nanostructures through post-processing techniques, such as acid etching and ligand exchange[46-48].

### Bottom-up method

*Soft-template method*

The soft-template method involves the cooperative assembly of amphiphilic surfactants, metal precursors, and organic ligands during the crystallization process of MOFs. Subsequently, the templates are removed through washing, forming meso-/macropore structures within a microporous MOF matrix[49]. In this method, MOF precursors are assembled with surfactants through electrostatic or hydrogen bonding interactions. Simultaneously, the meso-/macropore sizes are contingent upon the dimensions of the hydrophobic micellar cores and, thus, can be modified by tuning the chain length of hydrophobic segment of block copolymer surfactants or introducing pore-swelling agents such as toluene, 1,3,5-trimethylbenzene (TMB), *etc.*[50].

Liu and Hudson used block copolymer polystyrene-poly(ethylene oxide) (PS-*b*-PEO) as the template to prepare hierarchical porous MOF [HP-MOF ZnICA (ICA = 2-imidazolecarboxaldehyde)] through solvent evaporation-induced co-assembly [Figure 2A][51]. The resulting MOF monoliths possess meso-/macropores ranging from 40 to 95 nm [Figure 2B-E]. During the reaction, the MOF precursor co-assembles with PS-*b*-PEO micelles and grows within the gaps of the micelles. The subsequent heat treatment causes the melting of poly(ethylene oxide) (PEO) segments, resulting in micelle fusion to form larger pores. This evaporation-induced self-assembly approach can also be extended to synthesize other hierarchical MOF materials.

Compared to the evaporation-induced method, aqueous reaction systems are more conducive to producing uniform and dispersed MOF crystals with increasingly controllable pore/nanostructures[52-54]. The advantages of aqueous synthesis include enhanced precision in regulating the ordering, dimensions, and shapes of pore channels and the morphology of MOF particles[55]. As depicted in Figure 2F, Li *et al.* demonstrated a salt-mediated strategy to synthesize hierarchically mesoporous Ce-based MOFs using either the surfactant P123 or F127 as soft templates (denoted as Ce-HMMOF-P/Ce-HMMOF-F)[49]. Ce-HMMOF-P particles synthesized with P123 as the soft template exhibit highly open and uniformly ordered tubular channels [Figure 2G and H]. The Ce-HMMOF-F synthesized with F127 as the template possesses truncated octahedral morphology with ordered face-centered cubic (space group *Fm*3*m*) mesopores [Figure 2I and J]. In the MOF formation, the PEO segments in the surfactant show strong interaction with the metal clusters, thereby enabling the directed incorporation of organized micelles into MOFs and allowing for precise control over their mesopore structures.

In constructing hierarchically porous MOFs, introducing suitable oils as pore swelling agents into the reaction system to create an emulsion system can further regulate the mesopore size in MOF particles and even alter their morphologies. Li *et al.* synthesized a series of hierarchical MOFs (UiO-66-$NH_2$) with different pore sizes and morphologies through salt-assisted nanoemulsion-guided assembly [Figure 3A][56]. By varying the feeding ratio of two similar surfactants (P123/F127) and the amount of oil phase introduced simultaneously, the structure of MOF particles undergoes corresponding changes, forming structures such

**Table 1. Different strategies used to prepare hierarchical MOF nanoarchitectures**

| Typical example | | Routes | Structural feature | Ref. |
|---|---|---|---|---|
| ZnICA | Bottom-up method | Soft-template method | Meso-/macroporous monoliths | [51] |
| UiO-66(Ce) | | | Ordered mesoporous nanoparticles | [49] |
| UiO-66-$NH_2$(Zr) | | | Bowl-like particles, nanodisks, *etc.* | [56] |
| UiO-66(Ce) | | | Dendritic meso-/macropores nanoparticles | [57] |
| ZIF-8 | | Hard-template method | Ordered bicontinuous-structured cubosomes | [60] |
| ZIF-8 | | | Ordered macroporous nanoparticles | [45] |
| ZIF-8 | | | Two-dimensional superstructural sheets | [63] |
| Cu-BDC | | Mixed-template method | Meso-/macroporous nanoparticles | [64] |
| UiO-66(Ce) | | | Dual-mesoporous nanoparticles | [65] |
| UiO-66(Ce) | | | Hollow mesoporous nanoparticles | [66] |
| UiO-66-$NH_2$(Zr) | | | Two-dimensional meso-/macroporous nanosheets | [32] |
| ZIF-67 | | | Nanobowls with mesoporous core | [70] |
| PCN-222/PCN-608 | | Template-free method | Nanorods on ellipsoid heterostructural nanoparticles | [78] |
| MIL-88B/UiO-66 | | | Rods-on-octahedron heterostructural nanoparticles | [79] |
| UiO-66/MIL-125 | | | One-dimensional superstructural chains | [80] |
| ZIF-67 | Top-down method | Acid etching method | Nanoframes | [83] |
| MIL-101(Al, Cr) | | | Mesoporous hollow nanoparticles | [85] |
| UiO-66-$NH_2$(Zr) | | | Mesoporous multi-shell hollow nanoparticles | [22] |
| Cu-BTC | | Ligand-exchange method | Two-dimensional nanosheets | [89] |
| UiO-66(Zr) | | | Defective mesoporous nanoparticles | [90] |
| Cu-BHT | | | Nanoboxes | [91] |
| ZIF-8 | | | Yolk-shell nanocubes, ball-in-box nanocubes, *etc.* | [92] |
| ZIF-L | | Other method | Nanoframes | [95] |
| MOF-5 | | | Plus-shaped and fractal-patterned porous nanosheets | [96] |
| UiO-66(Zr) | | | Nanocages | [97] |
| ZIF-71 | | | Patterned films | [98] |

MOF: Metal–organic framework; ICA: 2-imidazolecarboxaldehyde; ZIF: zeolitic imidazolate framework; BDC: 1,4-benzenedicarboxylate; PCN: porous coordination network; MIL: Materials Institute Lavoisier; BTC: trimesic acid; BHT: benzenehexathiol.

as bowl-like particles, dendritic nanospheres, walnut-shaped particles, crumpled nanosheet, and nanodisk [Figure 3B-F]. This is because the nanoemulsion, which serves as the template to induce MOF assembly, is influenced by both surfactants and the oil phase, thereby further altering the pore size and morphology of MOFs. Increasing the ratio of P123 to F127 favors the combination between surfactants and the oil phase, resulting in larger nanoemulsion and thus larger pore sizes. With the volume increase of the nanoemulsion, it is easier to deform and fuse during the stirring process, and shape changes of the nanoemulsion could also lead to variations in morphology of the resultant MOFs.

By rationally manipulating the cooperative assembly process in oil/water emulsion systems, the precise control of particle structural symmetries, pore sizes and particle diameters can be achieved. Our research group synthesized 3D dendritic hierarchically porous MOF (UiO-66) nanoparticles (DHPNPs) through a non-centrosymmetric pore-induced anisotropic assembly strategy in an oil/water emulsion system [Figure 3G][57]. The bent MOF nanosheets, with a thickness of approximately 5 nm, construct highly open dendritic meso-/macropores. The unique formation process starts from anisotropic nucleation of MOF spherical nanocones through assembly of polymer surfactant P123, pore swelling agent TMB, and MOF precursors. As the reaction progresses, the nanocones grow radially and azimuthally. After the mass transfer gradually slows down due to increasing system viscosity, the preferential radial growth decelerates while the


**Figure 1.** Different strategies used to prepare hierarchical MOF nanoarchitectures. MOF: Metal–organic framework.

growth rate of the polar angle increases, finally forming isotropic spheres [Figure 3H-M]. Moreover, the pore size and particle diameter of MOFs can be systematically adjusted by changing the reaction temperature and the amount of MOF precursors introduced into the reaction systems. As the reaction temperature rises, the PEO units in P123 partially dehydrate, diminishing the volume of the hydrophilic corona, which leads to a thinner pore wall and a larger pore diameter. When the ligand content in the reaction system is lowered, the growth rates of the radius and solid angle of MOF particles also slow, resulting in a smaller average size of MOF particles, and the nanostructure changes from a sphere to an incomplete spherical cone.

*Hard-template method*

The hard-template method is another approach to constructing hierarchical nanostructures of MOFs. Unlike soft-template strategy, it employs rigid templates, which offer higher stability and more effective restraint ability, thereby strictly controlling the internal nanostructure of MOFs. Subsequently, selective template removal yields MOFs with inverse replica structures[58,59].

Using the hard-template method, MOF structures with ordered meso-/macropores and controllable pore sizes can be synthesized more easily. As a typical example, Li *et al.* demonstrated the synthesis of ordered bicontinuous-structured MOF [zeolitic imidazolate framework (ZIF)-8] using polymer cubosomes [Figure 4A][60]. Using self-assembled double primitive structured cubosomes as templates, MOF precursor adsorption occurs inside the pores through capillary action and intermolecular interactions. After *in situ* growth, the template is removed by washing with tetrahydrofuran, resulting in MOF cubes with a single primitive structure (denoted as SP-ZIF-8). SP-ZIF-8 exhibits a regular tetragonal pore array with an average pore diameter of 65 nm and a wall thickness of 25 nm [Figure 4B and C]. Unlike the traditional growth of ZIF-8, SP-ZIF-8 adopts a fast 3D heterogeneous growth mode. Furthermore, this universal method can also

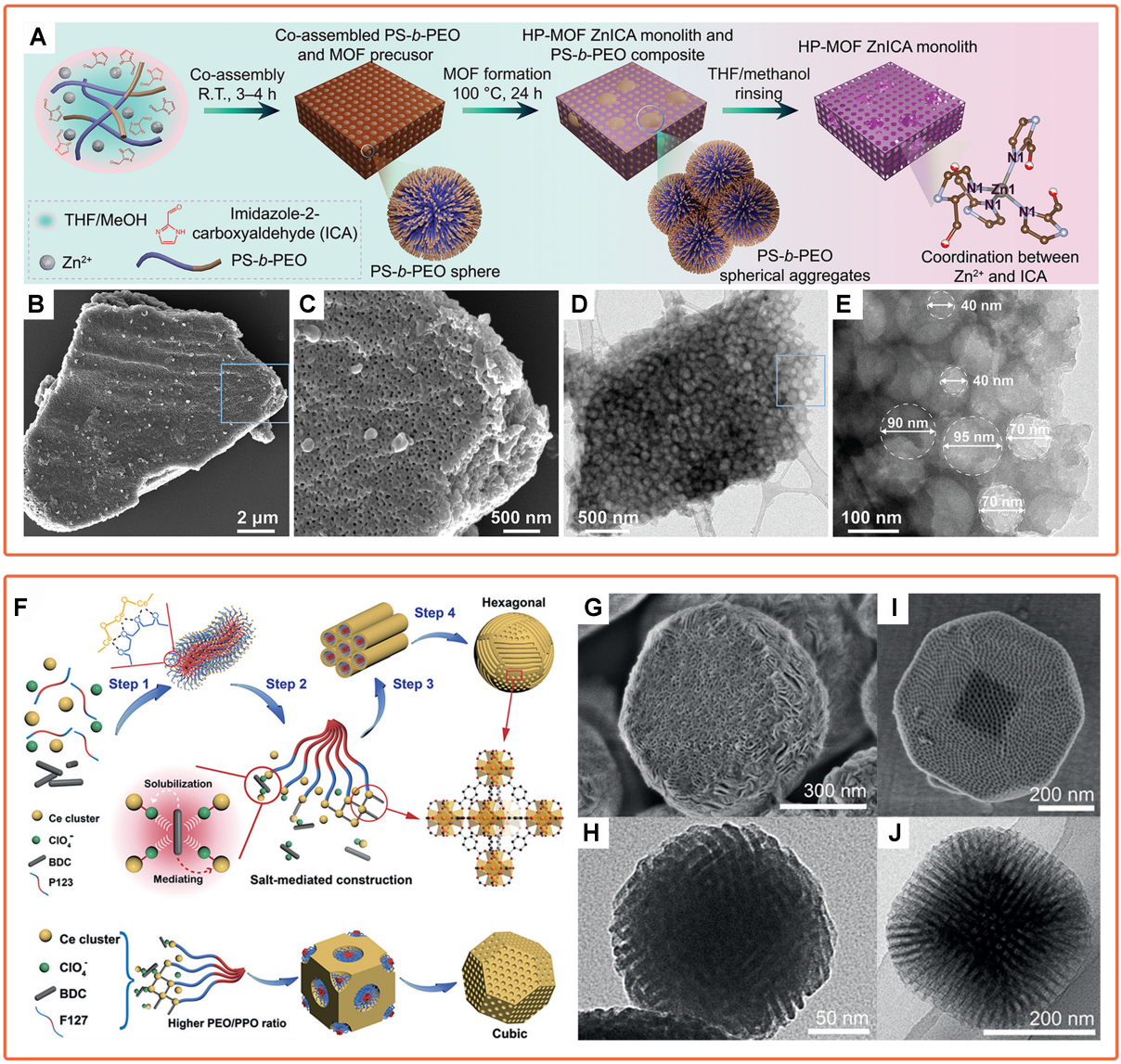


**Figure 2.** (A) Formation process of HP-MOF ZnICA monoliths; (B and C) SEM images and (D and E) TEM images of HP-MOF ZnICA monoliths[51]. Copyright 2023, Wiley-VCH; (F) Schematic illustration of the formation mechanism of ordered large-pore Ce-HMMOF-P and Ce-HMMOF-F; (G and I) SEM and (H and J) TEM images of (G and H) Ce-HMMOF-P and (I and J) Ce-HMMOF-F[49]. Copyright 2020, Wiley-VCH. HP-MOF: hierarchical porous metal–organic framework; ICA: 2-imidazolecarboxaldehyde; SEM: scanning electron microscopy; TEM: transmission electron microscopy.

be used to synthesize ZIF-67 and copper-benzene-1,3,5-tricarboxylate (HKUST-1) with a single primitive structure.

In another study, Shen *et al.* used highly ordered 3D polystyrene (PS) monoliths as hard templates and synthesized 3D single-crystal ordered macroporous MOF (denoted as SOM-ZIF-8) using a double-solvent-induced heterogeneous nucleation method [Figure 4D][45]. The macropores of 270 nm are arranged in an orderly manner on the six square planes and eight triangle planes of SOM-ZIF-8, corresponding to the {100} and {111} planes of the PS template, respectively [Figure 4E and F]. During the preparation process, MOFs grow *in situ* within the ordered pores of the template. After the reaction, PS is selectively removed using tetrahydrofuran. Furthermore, using PS spheres with different diameters, precise control of the macropore

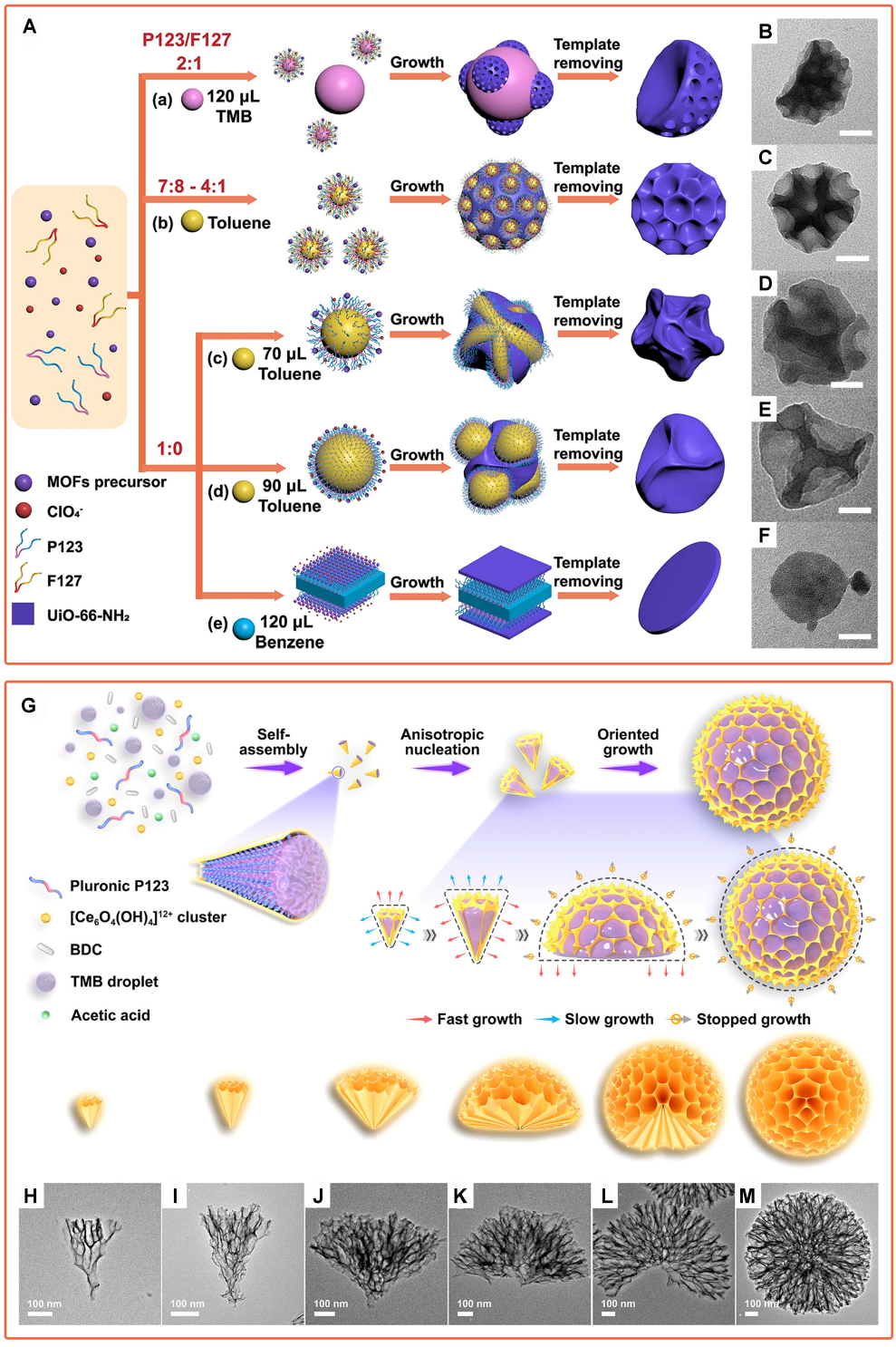


**Figure 3.** (A) Formation of hierarchical Zr-based MOFs with various architectures using the proposed nanoemulsion-guided assembly strategy; (B-F) TEM images of UiO-66-$NH_2$. (B) bowl-like particle; (C) dendritic nanosphere; (D) walnut-shaped particle; (E) crumpled nanosheet; and (F) nanodisk[56]. Copyright 2022, Springer Nature; (G) Schematic illustration of the formation process of UiO-66 DHPNPs; (H-M) TEM images of UiO-66 nanostructures prepared with different reaction durations: (H) 11.5; (I) 15; (J) 19; (K) 22; (L) 39; and (M) 50 min[57]. Copyright 2023, American Chemical Society. Scale bars: (B-F) 50 nm. MOFs: Metal–organic framework; TEM: transmission electron microscopy; DHPNPs: dendritic hierarchically porous MOF (UiO-66) nanoparticles.

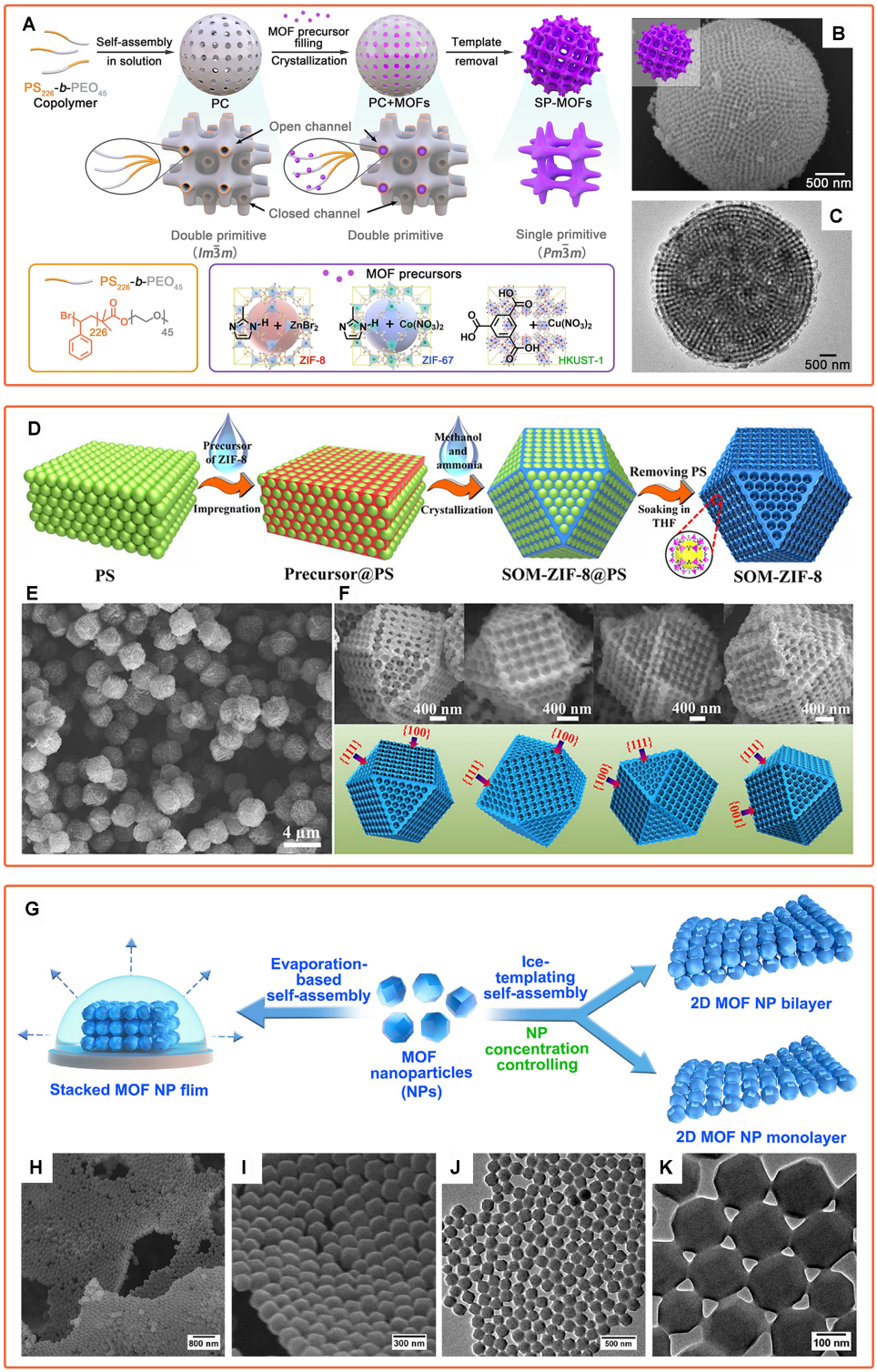


**Figure 4.** (A) Formation of SP-MOF cubosomes; (B) SEM and (C) TEM images of SP-ZIF-8[60]. Copyright 2023, Wiley-VCH; (D) Schematic illustration of the formation route of SOM-ZIF-8; (E) Low-magnification SEM image and (F) SEM images taken from different directions of SOM-ZIF-8[45]. Copyright 2018, the American Association for the Advancement of Science; (G) Schematic illustration of evaporation-based self-assembly and ice-templating self-assembly; (H and I) SEM images and (J and K) TEM images of the TR-Z8-1 monolayer[63]. Copyright 2022, American Chemical Society. MOF: Metal–organic framework; SEM: scanning electron microscopy; TEM: transmission electron microscopy; ZIF: zeolitic imidazolate framework.

sizes can be achieved. This versatile method could also be expanded to fabricate hierarchically porous structures of various other MOFs[61,62].

In addition to pre-prepared templates, the hard templates formed during the reaction can also effectively serve as constraints. In a recent study by Song *et al.*, two-dimensional (2D) layered truncated rhombic dodecahedral ZIF-8 nanoparticle superstructures (denoted as TR-Z8-1) were constructed by an ice-templating strategy [Figure 4G][63]. The prepared superstructure is self-assembled by ZIF-8 to form a uniform 2D sheet-like structure [Figure 4H-K]. During the cooling process, ice gradually forms, causing the MOF particles in the solvent to be slowly pushed towards the boundaries between ice crystals, where the MOFs are brought together through Vander Waals forces. By altering the initial solution concentration, the transformation of the 2D sheets from monolayer to bilayer structures can be achieved.

*Mixed-template method*

The mixed-template method combines various types of templates for constructing MOF nanostructures. By controlling the growth kinetics of MOFs, different templates can fulfill their respective functions, introducing multiple structural characteristics into the MOF particles simultaneously[22]. For example, hierarchical meso-/macropore structures can be introduced into the MOF matrix using both soft and hard templates. Highly ordered macroporous-mesoporous Cu-1,4-benzenedicarboxylate (BDC) (Macro-Meso-Cu-BDC) structures were synthesized by combining hard-template PS monoliths and soft template P123 through solvent evaporation-induced co-assembly [Figure 5A][64]. The macropores, with a diameter of 265 nm, arrange in a face-centered cubic manner after removing the hard template, while the mesopores, with a diameter of 4.1 nm, assemble orderly by the soft template, exhibit a periodic hexagonal structure [Figure 5B-E].

In addition to the mixed-template strategy by integrating soft and hard templates, a dual-soft-template approach has also been used to construct unique MOF nanostructures. Li *et al.* synthesized core-shell structured dual-mesoporous Ce-based MOFs (denoted as DMCM-CL1F3) by employing two distinct copolymer templates in the reaction system [Figure 5F][65]. The structure includes large mesopores of 24 nm formed by poly(ethylene oxide)-*b*-poly(caprolactone) (PEO-*b*-PCL) directed assembly in the inner core and small mesopores of 9.5 nm formed by F127 directed assembly in the outer shell [Figure 5G and H]. During the addition of water in the reaction, the hydrophobicity of the PCL segment causes the enrichment of acetone around the PEO-*b*-PCL micelles. The property of acetone easily dissolves the MOF ligands, increasing the growth rate of the surrounding MOF, thereby preferentially generating the large mesopores within the inner core. Subsequently, F127 further assembles to form the small mesopores in the outer shell. It is worth noting that by changing the ratio of the two surfactants and the acetone concentration, variations in the thickness of the core and shell can be achieved.

Moreover, in the emulsion systems, the oil phase not only serves as a pore-swelling agent but, when properly controlled, can also function similarly to a soft template, which could combine with traditional surfactant soft templates to construct nanostructures with additional structural features. Zhao *et al.* developed a kinetically mediated micelle assembly strategy for synthesizing hollow mesoporous UiO-66(Ce) single crystals [denoted as HMS UiO-66(Ce)] with radially arranged mesoporous shells [Figure 6A][66]. The MOF particles possess large cavities of 450 nm and radially aligned mesopores of 25 nm [Figure 6B-D]. The formation of the hollow mesoporous structure is due to the reduction in the concentration of free Ce ions by increasing the content of the modulator acetic acid in the emulsion system. Their induced decrease in the concentration of UiO-66 oligomers falls below the threshold required for homogeneous self-assembly, thus facilitating the heterogeneous self-assembly of micelles at the oil-water interface. Additionally, adjusting the

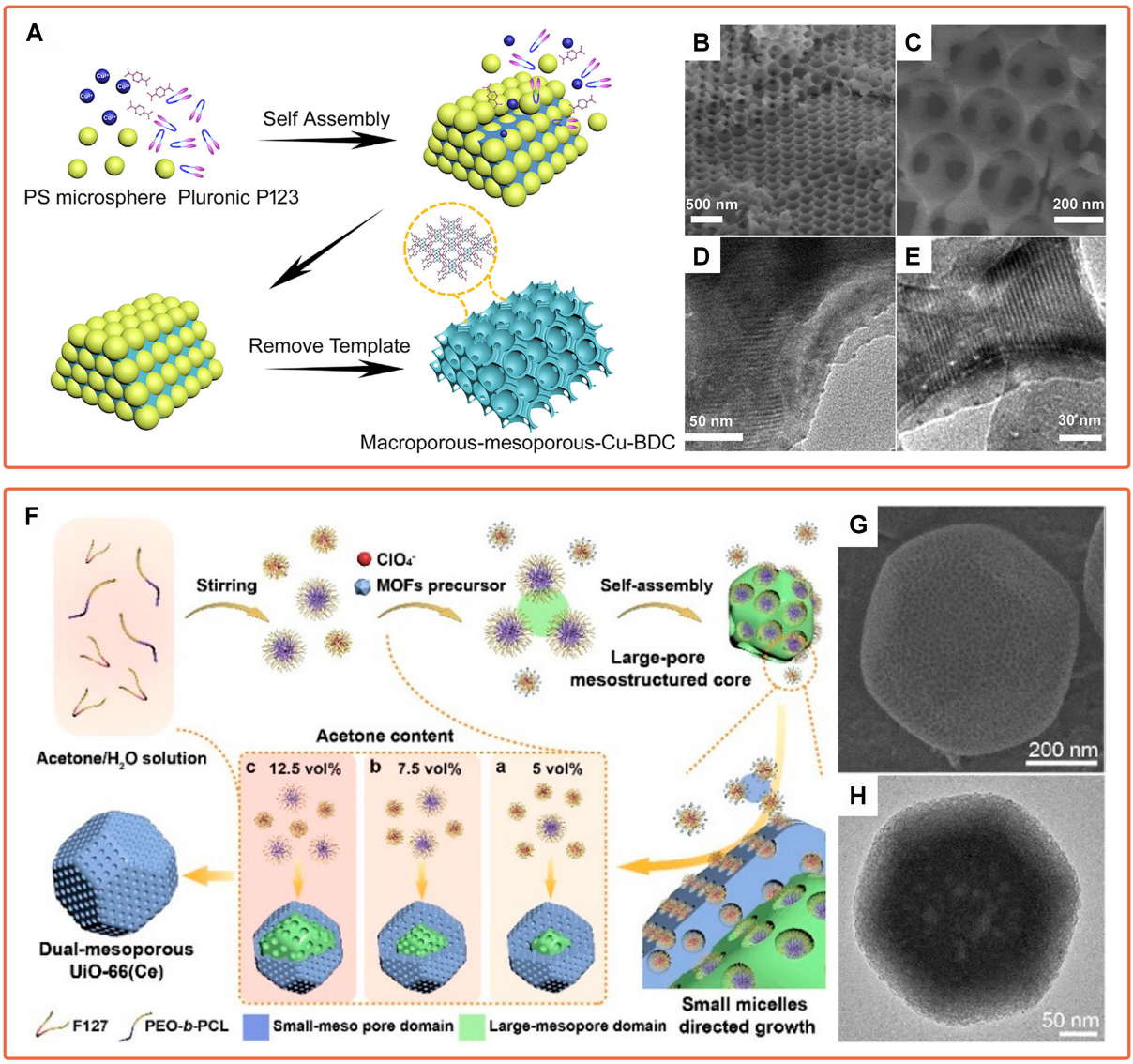


**Figure 5.** (A) Formation process of Macro-Meso-Cu-BDC; (B and C) SEM images and (D and E) TEM images of Macro-Meso-Cu-BDC[64]. Copyright 2019, Elsevier B.V; (F) Schematic illustration of the formation of DMCM-CL1F3; (G) SEM and (H) TEM images of DMCM-CL1F3[65]. Copyright 2024, American Chemical Society. BDC: 1,4-benzenedicarboxylate; SEM: scanning electron microscopy; TEM: transmission electron microscopy; DMCM: dual-mesoporous Ce-based MOFs.

ratio of F127/P123 enables the pore structural transition from radially arranged mesopores to cage-like mesopores.

In a recent study, our group demonstrated a "hard" emulsion-induced interface super-assembly strategy for the synthesis of 2D UiO-66-$NH_2$ hierarchically porous nanosheets (denoted as 2D UiO-66-$NH_2$ HPNSs)[32]. The prepared nanosheets exhibit a sheet-like structure with a thickness of ~28 nm, an average diameter of 1.5 μm, and uniform mesopores of ~8 nm [Figure 6E and F]. The nanosheets formed by the crystallization of *n*-octadecanol and F127 during the cooling process serve as "hard" emulsion templates. In the reaction process, octadecyl dimethyl betaine (ODMB) gradually replaces F127 on the surface of the emulsion templates due to the "like dissolves like" principle. Through the strong coordination interaction between ODMB and Zr-oxo cluster, the mesoporous MOF nanocrystals formed by block copolymer F127 and the

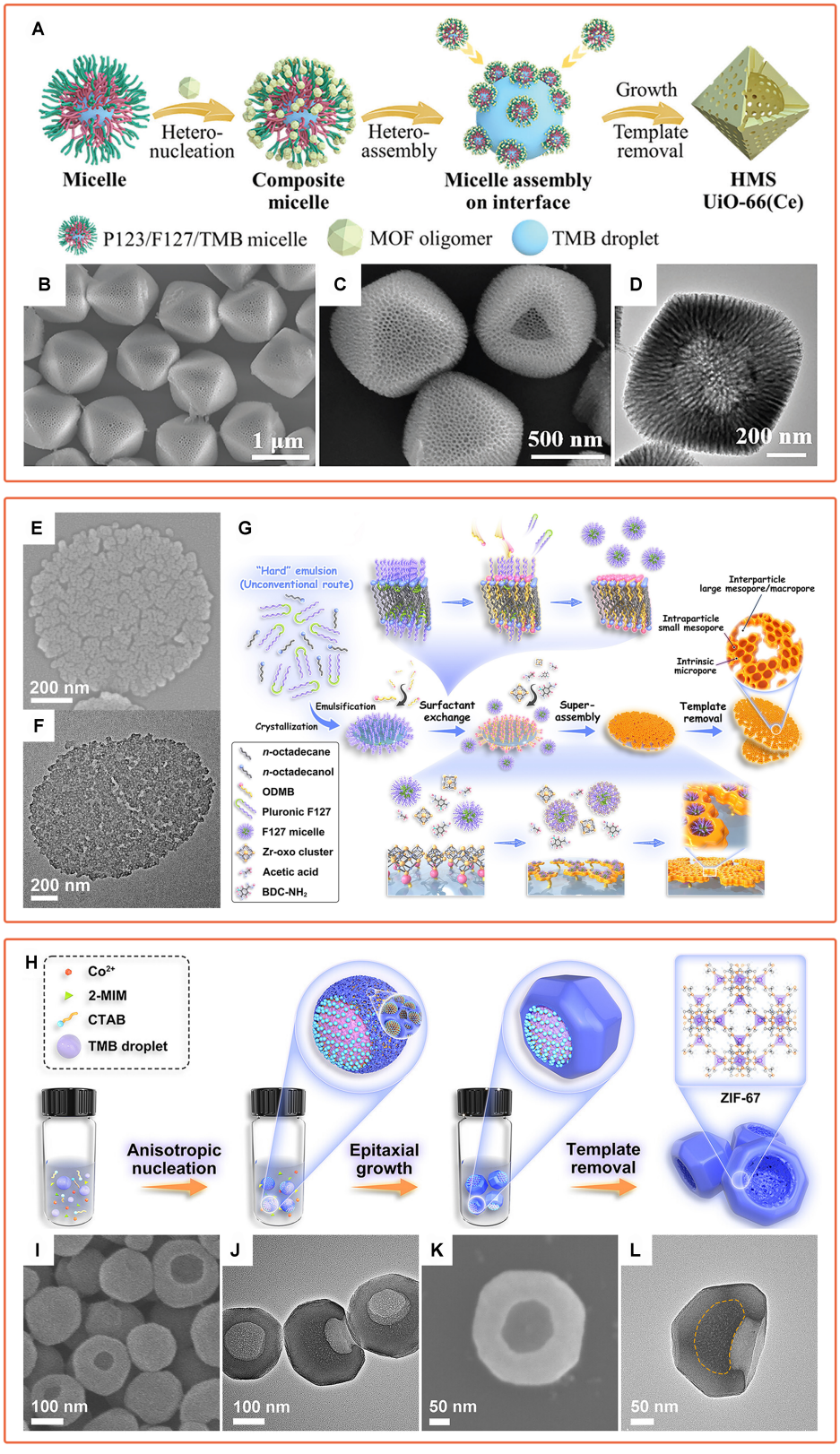


**Figure 6.** (A) Formation mechanism of HMS UiO-66(Ce); (B and C) SEM images and (D) TEM image of HMS UiO-66(Ce)[66]. Copyright 2023, Wiley-VCH; (E) SEM and (F) TEM images of 2D UiO-66-$NH_2$ HPNSs; (G) Formation mechanism of the 2D "hard" emulsion-induced interface super-assembly strategy[32]. Copyright 2024, American Chemical Society; (H) Schematic illustration of the

formation process of ZIF-67 meso-/microNBs; (I and J) SEM and (K and L) TEM images of ZIF-67 meso-/microNBs[70]. Copyright 2023, American Chemical Society. SEM: scanning electron microscopy; TEM: transmission electron microscopy; 2D: two-dimensional; ZIF: zeolitic imidazolate framework.

MOF precursors are assembled on the 2D emulsion templates to form 2D UiO-66-$NH_2$ HPNSs through heterogeneous nucleation and growth [Figure 6G]. In addition, the hierarchical pore sizes of the MOF nanosheets can be adjusted by changing the amounts of mesopore swelling agents and coordination modulators in the reaction systems. It is also worth noting that this strategy can prepare other types of 2D MOF hierarchically porous nanosheets.

Besides constructing centrosymmetric MOF nanostructures, there is also considerable interest in designing anisotropic geometric structures with noncentrosymmetry[67,68]. For example, asymmetric MOF nanobowls could offer enhanced packing density, higher specific surface area, and improved mass/ionic transfer capability[69]. Our group demonstrated an anisotropic interface successive assembly method for synthesizing asymmetric core-shell structured ZIF-67 nanobowls (denoted as ZIF-67 meso-/microNBs, Figure 6H)[70]. The bowl-shaped particles with an average diameter of 250 nm have an asymmetric core-shell structure, consisting of a mesoporous hemispherical bowl bottom and a microporous polyhedral shell [Figure 6I-L]. In this system, cetyltrimethylammonium bromide (CTAB) collaborates with TMB to stabilize the emulsion droplets and enhance the interface interaction between MOF precursors and droplets, leading to anisotropic nucleation. Excessive CTAB in water contributes to the formation of swelling micelles, which assemble with MOF precursors to generate hemispherical cores with worm-like mesopores on emulsion droplets. After the depletion of CTAB, continuous epitaxial growth on each mesoporous hemisphere and emulsion droplet leads to the oriented formation of a microporous ZIF-67 shell.

*Template-free method*

In the absence of template assistance, MOF particles typically exhibit specific, regular morphologies, such as regular rhombic dodecahedra of ZIF-8 and octahedra of UiO-66. In this scenario, the construction of MOF nanostructures can rely on the anisotropic epitaxial growth resulting from the similarity in lattice parameters between MOFs along specific directions, forming MOF-on-MOF heterostructures[71-74]. Compared to single MOFs, heterogeneous MOF-on-MOF composite materials exhibit unique functional tunability and hierarchical nanostructures, which can simply integrate and customize the functions of MOFs[75-77].

In recent research by Zhao *et al.*, a series of hierarchical low-dimension MOF heterostructures were synthesized using a seed-mediated epitaxial growth method [Figure 7A][78]. In these structures, one-dimensional (1D) porous coordination network (PCN)-222 nanorods could selectively grow either along the major axis of zero-dimensional (0D) ellipsoidal PCN-608 particles, at both two ends of 1D NU-1000 nanorods, or perpendicular to both sides of 2D PCN-134 nanoplates to form 1D/0D, 1D/1D, and 1D/2D heterostructures [Figure 7B-D]. Moreover, 2D Zr-1,3,5-tris(4-carboxyphenyl)benzene (BTB) nanosheets could also selectively grow along the edges of 2D PCN-134 nanoplates, resulting in the formation of 2D/2D heterostructures [Figure 7E]. Due to the different ligands and topological structures of the two MOFs in each MOF heterostructure, the secondary MOF can only epitaxially grow on specific surfaces of the seed MOF with small lattice mismatches, resulting in a series of MOF composites with various hierarchical architectures. Similarly, Wang *et al.* designed a unique 3D rods-on-octahedron MOF heterostructure[79]. The nanoparticles consist of an octahedral core (UiO-66) and hexagonal rods Materials Institute Lavoisier (MIL)-88B growing on each of the eight faces. Each MIL-88B rod is perpendicular to each face of the UiO-66 octahedron, and the rectangular side face of hexagonal MIL-88B is parallel to one side of the

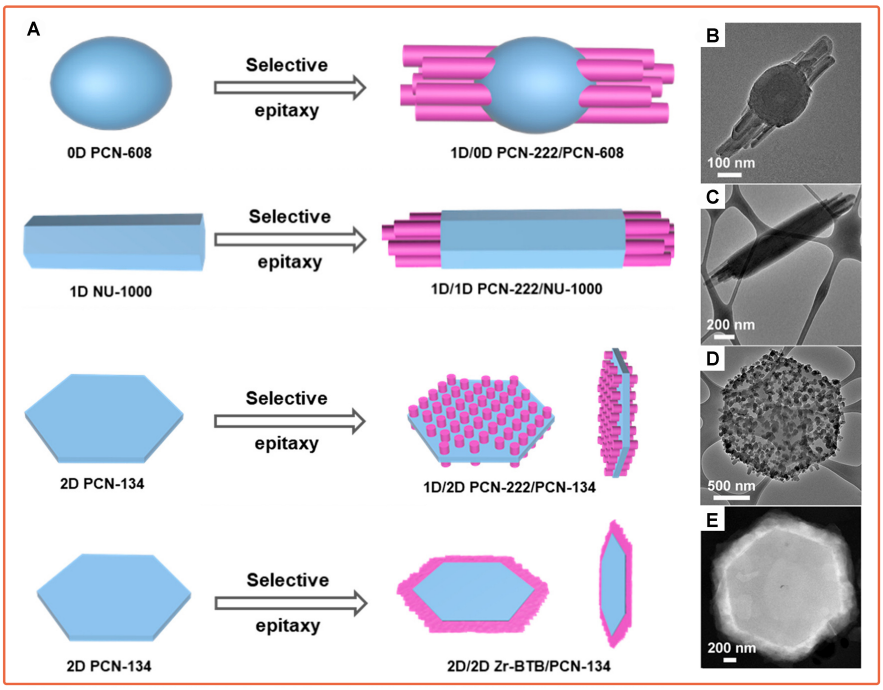
A
Selective
epitaxy
0D PCN-608
1D/0D PCN-222/PCN-608
1D NU-1000
1D/1D PCN-222/NU-1000
2D PCN-134
1D/2D PCN-222/PCN-134
2D PCN-134
2D/2D Zr-BTB/PCN-134
B
100 nm
C
200 nm
D
500 nm
E
200 nm

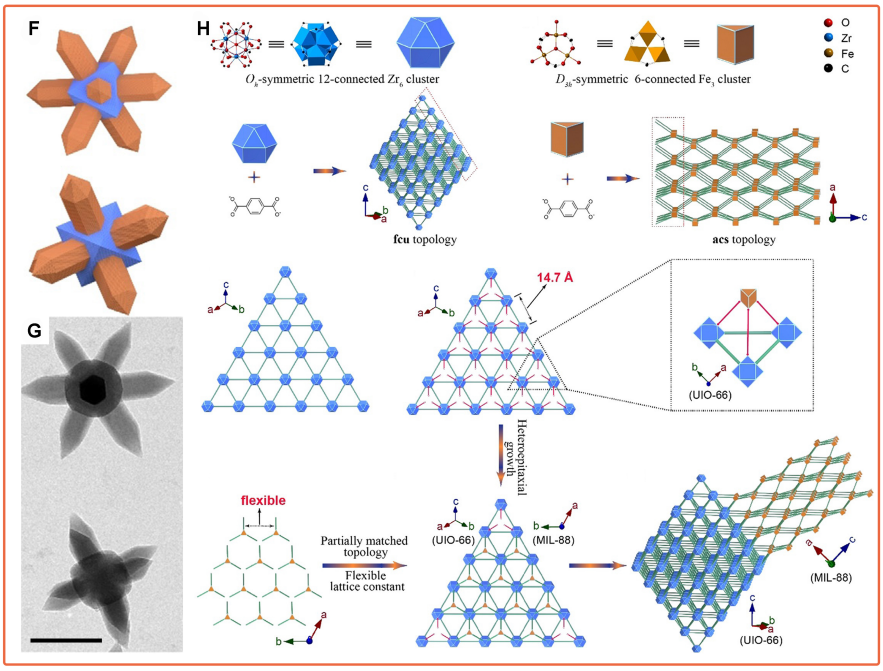
F
G
H
O
Zr
Fe
C
fcu topology
acs topology
14.7 Å
(UIO-66)
Heteroepitaxial growth
flexible
Partially matched topology
Flexible lattice constant
(UIO-66)
(MIL-88)
(MIL-88)
(UIO-66)

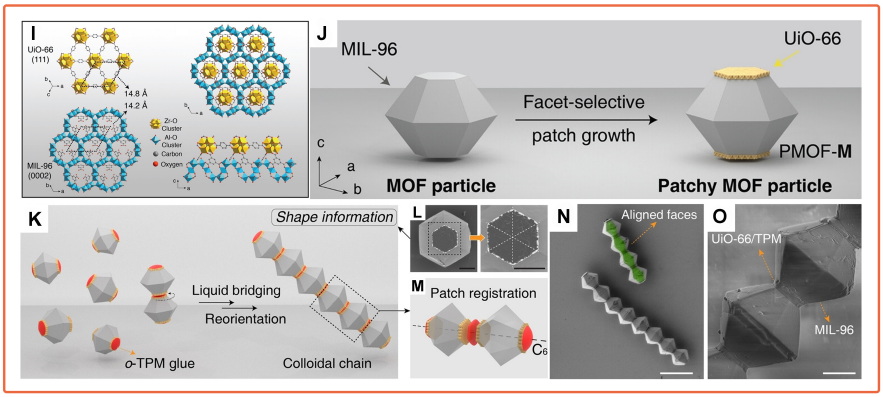
I
J
MIL-96
UiO-66
Facet-selective
patch growth
PMOF-M
MOF particle
Patchy MOF particle
K
Shape information
Liquid bridging
Reorientation
o-TPM glue
Colloidal chain
L
M
Patch registration
N
Aligned faces
O
UiO-66/TPM
MIL-96

**Figure 7.** (A) Formation of various heterostructures by selective epitaxial growth; (B-E) TEM images of (B) 1D/0D PCN-222/PCN-608; (C) 1D/1D PCN-222/NU-1000; and (D) 1D/2D PCN-222/PCN-134; (E) STEM image of 2D/2D Zr-BTB/PCN-134[78]. Copyright 2020, American Chemical Society; (F) 3D models and (G) TEM images of MIL-88B-on-UiO-66; (H) Schematic illustration of the formation mechanism of MIL-88B-on-UiO-66[79]. Copyright 2020, Wiley-VCH; (I) Top and side views of the crystal structures of the (111) plane of UiO-66 and the (0002) plane of MIL-96; (J) Formation of PMOF-M; (K-M) Schematic illustration of the fabrication procedure for PMOF-M chains; (N and O) SEM images of PMOF-M chains[80]. Copyright 2021, Wiley-VCH. Scale bars: (G) 200 nm, (L) 2 μm, (N) 10 μm, and (O) 2 μm. TEM: Transmission electron microscopy; 1D: one-dimensional; 0D: zero-dimensional; PCN: porous coordination network; 2D: two-dimensional; STEM: scanning transmission electron microscopy; BTB: 1,3,5-tris(4-carboxyphenyl)benzene; 3D: three-dimensional; MIL: Materials Institute Lavoisier; PMOF-M: patchy MOF heterostructures with medium-sized matrix and patches; SEM: scanning electron microscopy.

triangular face of the octahedron [Figure 7F and G]. This is due to partial matching of the two MOF lattices, and the MIL-88B with **acs** topology (a hexagonal net of aligned, corner-sharing trigonal prisms) utilizes the flexibility of its own structure to compensate for the differences in lattice parameters [Figure 7H].

After forming MOF heterostructures through the anisotropic epitaxial growth of MOFs, more interesting structures can be prepared through further super-assembly processes. Lyu *et al.* used an *in situ* strategy employing 3-(trimethoxysilyl)propyl methacrylate (TPM) as a liquid glue to assemble patchy MOF heterostructures with medium-sized matrix and patches (PMOF-M) into 1D superstructures[80]. The (111) plane of UiO-66 closely matches the (0002) plane of MIL-96 [Figure 7I and J]; thus, UiO-66 can selectively grow in the (0002) plane of MIL-96 to form PMOF-M. By changing the solvent, TPM can selectively nucleate only on the UiO-66 surface. Under stirring, the particles rapidly reorient and gradually assemble into 1D superstructures [Figure 7K-O].

### Top-down method

*Acid etching method*

By meticulously designing and constructing MOFs with uneven framework stability, followed by acid etching to remove unstable frameworks, the nanostructure of MOFs can be effectively modulated[81,82]. Cai *et al.* synthesized hollow-structured MOF (ZIF-67) nanoframes through selective modification and etching[83]. Using the truncated ZIF-67 (tZIF-67) rhombic dodecahedron as the template, six {100} facets of tZIF-67 are completely removed, leaving only twelve hexagonal {110} facets selectively preserved [Figure 8A]. In the synthesis process, the proton and anionic ligand in cyanuric acid (CA) serve as an etchant and a protective agent, respectively. On the one hand, CA molecules can easily enter the {110} facets of ZIF-67 with larger pores, where they are moderately coordinated with cobalt ions to protect the {110} facets of the MOF from etching. On the other hand, the {100} facets with higher atomic packing density and smaller pore size pose difficulty for CA to penetrate [Figure 8B]. Additionally, the steric hindrance effect caused by more ligands coordinating around cobalt ions makes it difficult for CA to interact with the {100} facets. Consequently, during the formation of coordination bonds between cobalt ions and CA in the {110} facets, protons in CA diffuse into the interior of ZIF-67, etching the {100} facets of the MOF from the inside out [Figure 8C-G].

In addition to the controlled preparation of MOF nanostructures by *in situ* protection and etching, MOF precursor particles with designed inhomogeneous frameworks can be constructed by controlling the synthesis process, and then hierarchical MOF nanostructures can be obtained by etching away the unstable MOF regions[84]. As depicted in Figure 8H, Qin *et al.* demonstrated a method involving boosted nucleation and selective etching to synthesize hollow mesoporous MIL-101 (denoted as HM-MIL)[85]. HM-MIL, with an average size of 230 nm, exhibits a truncated octahedral shape with a shell thickness of approximately 30 nm. By boosting the nucleation process, many small coordination polymer units quickly nucleate and aggregate in the initial synthesis stage, forming a core with more defects. Subsequently, a more robust MOF

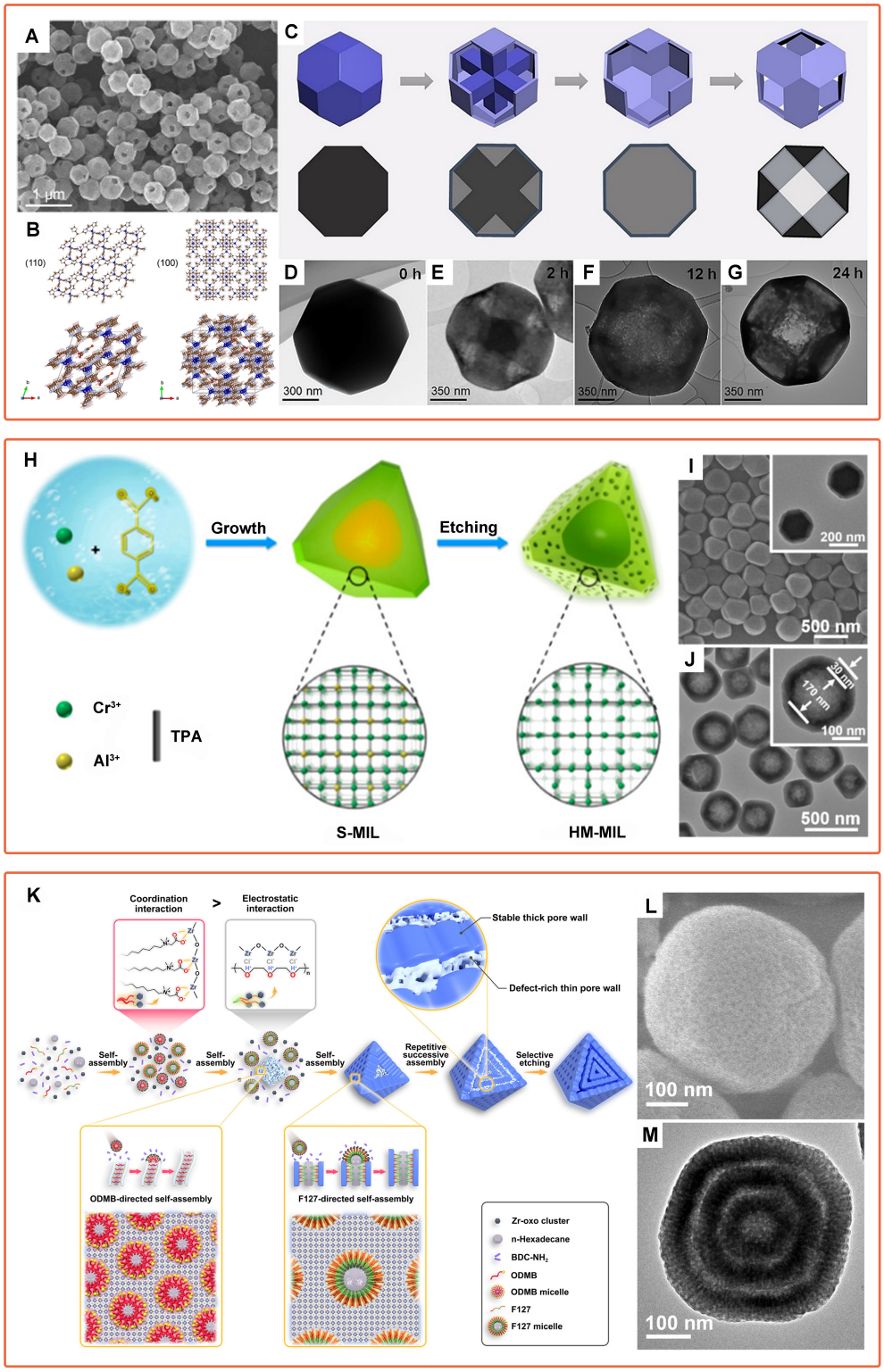


**Figure 8.** (A) Low-magnification SEM image of the tZIF-67 nanoframes; (B) Crystal structure of ZIF-67 along different directions; (C) Formation process and (D-G) corresponding TEM images of tZIF-67 nanoframes[83]. Copyright 2020, Wiley-VCH; (H) Schematic illustration of the formation process of HM-MIL; (I and J) SEM and TEM images of (I) S-MIL and (J) HM-MIL[85]. Copyright 2020, American Chemical Society; (K) Schematic illustration of the formation mechanism of 3S-mesoUiO-66-$NH_2$ HoMSs; (L) SEM and (M) TEM images of a 3S-mesoUiO-66-$NH_2$ HoMS[22]. Copyright 2023, Springer Nature. SEM: Scanning electron microscopy; ZIF: zeolitic imidazolate framework; TEM: transmission electron microscopy; MIL: Materials Institute Lavoisier.

shell gradually crystallizes and grows on the surface of the core [Figure 8I]. This results in a gradient-structured solid Cr, Al-bimetallic MIL-101 (S-MIL) with an unstable core and stable shell. The unstable core is selectively removed during etching to generate a hollow structure. Additionally, due to the stronger basicity of Al nodes compared to Cr nodes in the MOF shell, they are more easily removed under the treatment of acetic acid, thereby forming mesoporous MOF nanoshells [Figure 8J].

Compared with single-layer hollow mesoporous structures, the multi-shell hollow mesoporous structures could offer more diversified compartmentalization environments and abundant heterogeneous interfaces, which can achieve stronger enrichment of reactants and higher catalytic efficiency[84,86]. In a recent study by our group, hollow multi-shell mesoporous UiO-66-$NH_2$ (denoted as nS-mesoUiO-66$NH_2$ hollow multi-shell structures (HoMSs), where n represents the number of shells) was synthesized through successive assembly with dual templates and selective etching [Figure 8K][22]. The synthesized MOF particles contain three layers of cavities and radial mesopores of 7 nm [Figure 8L and M]. The two surfactants used in the synthesis process play different roles. The ionic surfactant ODMB shows a stronger coordination interaction with the MOF precursor, forming a disordered worm-like mesoporous core. After the depletion of ODMB, F127 continues to assemble with the MOF to form an outer shell with ordered radial mesopores. After repeating this growth process three times, MOF particles with three layers of alternating non-uniform structures can be obtained. Under the post-treatment of acetic acid, the unstable disordered mesoporous core is selectively etched, forming a multilayered mesoporous MOF structure. Using this method, the number of layers in the multi-shell MOF can reach up to seven.

*Ligand-exchange method*

The ligand-exchange method is simple and convenient for synthesizing MOF nanostructures. In this method, seed MOFs with weakly bonded ligands are first synthesized as the initial templates. Subsequently, the original ligands are exchanged with other ligands through the differences in their coordination reaction kinetics. During the ligand exchange process, various nanostructures, such as hierarchical porous and hollow architectures, can be introduced within original solid MOFs[87,88].

Through reasonable ligand exchange, the transformation of MOF structure from 3D to 2D can be realized simply. In a recent study, Zhou *et al.* transformed a 3D bulk Cu-BTC MOF into a 2D Cu-based topological structure through $CO_2$ coordination-driven ligand exchange[89]. The sample treated with supercritical $CO_2$ is transformed into ultra-thin nanosheets with an average thickness of 3.7 nm, equivalent to six single-layer planes of 0.6 nm stacked together to reduce the surface energy [Figure 9A and B]. During the reaction, part of the BTC ligands dissociate, and others at the symmetric sites tend to dissociate to form a 2D honeycomb layer of **hcb** topology thermodynamically. The dissociation reduces $Cu^{2+}$ to $Cu^{+}$, and simultaneously, a strong charge transfer interaction occurs between the electron orbits of $CO_2$ and metal to form $^{*}CO_2^{\bullet-}$ radicals. The carboxyl intermediates formed by the reaction of $H^{+}$ with radicals can further coordinate with Cu ions to block the 3D space connectivity [Figure 9C].

In addition to low-dimensional nanostructures, HP-MOFs can also be obtained by simple monodentate ligand exchange. For example, Cai *et al.* developed a universal post-synthetic ligand substitution (PSLS) strategy to transform microporous MOFs into HP-MOFs (HP-UiO-66) containing defective mesopores [Figure 9D and E][90]. When the concentration of monodentate ligands in the reaction system is high enough, the equilibrium state of the original dissociation and reassembly of the MOF is disrupted. Some monodentate ligands replace the original ligands under kinetic effects, thus forming defective pores [Figure 9F and G]. As the concentration of monodentate ligands gradually increases, the equilibrium continuously shifts, gradually enlarging the pore space.

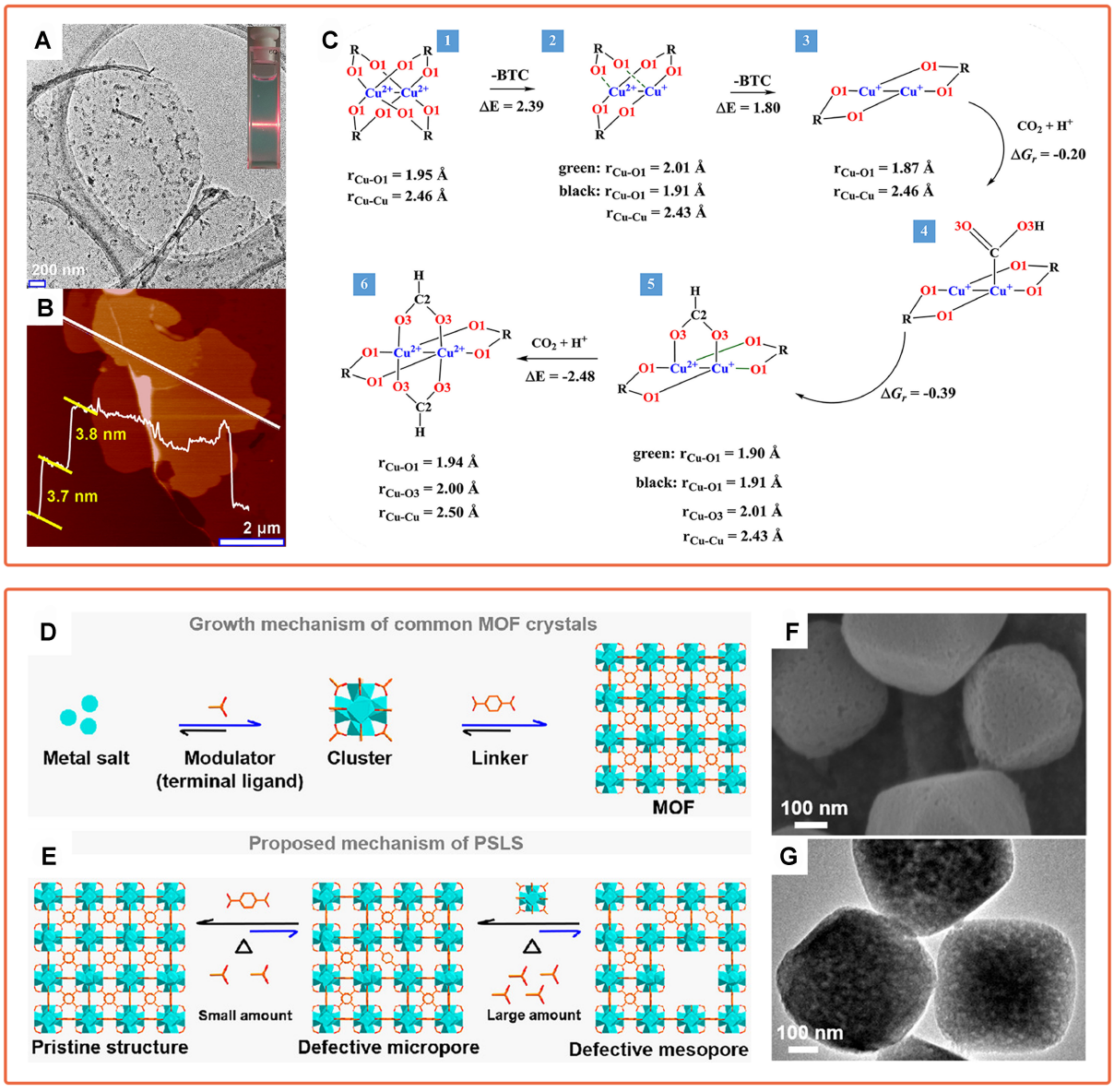


**Figure 9.** (A) TEM and (B) AFM images of 2D Cu-based topological structure; (C) The schematic illustration of molecular structures and energy evolution (ΔE) resulting from the local BTC ligands dissociation and the subsequent $CO_2$ coordination on Cu(II) dimer[89]. Copyright 2021, KeAi Communications Co., Ltd; Schematic illustration of (D) typical growth and (E) PSLS strategy; (F) SEM and (G) TEM images of HP-UiO-66[90]. Copyright 2021, American Chemical Society. TEM: Transmission electron microscopy; AFM: atomic force microscopy; 2D: two-dimensional; BTC: trimesic acid; PSLS: post-synthetic ligand substitution; SEM: scanning electron microscopy; $\Delta G_r$: reaction free energy.

Through rational design, MOFs can generate hollow nanostructures during ligand-exchange etching processes. In a recent study by Huang *et al.*, a series of highly crystalline hollow layer-stacked 2D conjugated MOFs (c-MOF) were synthesized using a ligand exchange template strategy [Figure 10A][91]. Given that many 2D c-MOF crystals have higher stability in acidic environments than 3D MOF crystals, traditional 3D MOFs with weak coordination bonds can be converted to 2D c-MOFs as sacrifice templates. The reaction process is divided into two steps. First, an amorphous c-MOF intermediate layer quickly forms on the MOF template surface. Subsequently, c-MOF crystals grow heterogeneously within the non-crystalline MOF, causing the central MOF template to gradually dissolve, resulting in a hollow structure [Figure 10B and C].

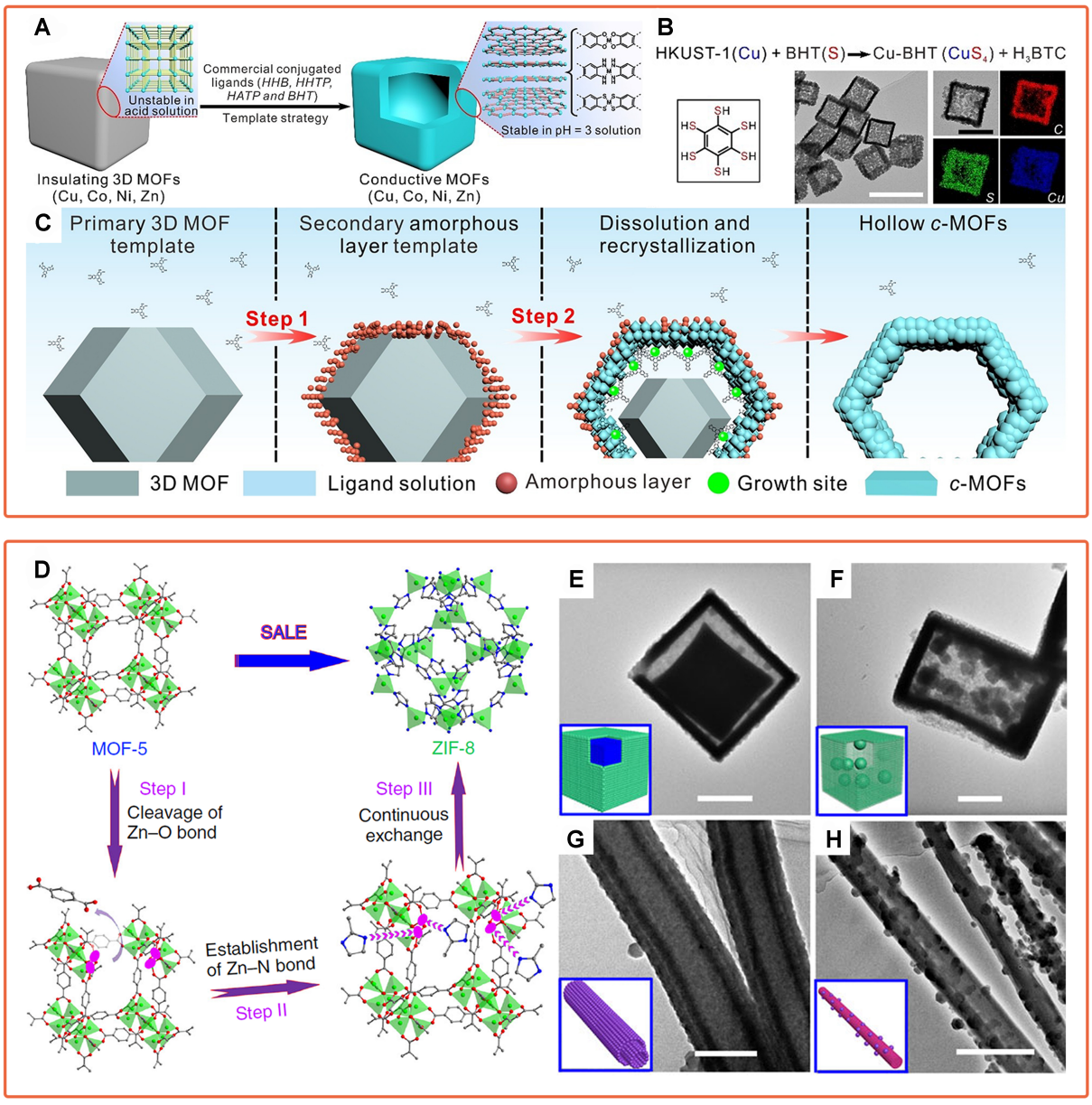


**Figure 10.** (A) Schematic illustration of the transformation from insulating 3D MOF precursors to layer-stacked 2D c-MOF samples; (B) Conjugated ligand (left), TEM image (middle) and the corresponding electron energy loss spectroscopy mapping (right) of hollow MOF nanocubes; (C) Schematic illustration of the formation mechanism of the two-stepped transformation mechanism of ZIF-8 particles to hollow particles[91]. Copyright 2023, Wiley-VCH; (D) Schematic illustration of a typical SALE process; TEM images of (E) yolk-shell nanocube, (F) ball-in-box nanocube, (G) ZIF nanotube, and (H) bead-on-string hybrid structure[92]. Copyright 2020, Springer Nature. Scale bars: (B) 500 nm for middle TEM image and 200 nm for right TEM images, (E) 400 nm, (F) 400 nm, (G) 500 nm, and (H) 500 nm. 3D: Three-dimensional; MOF: metal–organic framework; 2D: two-dimensional; c-MOF: conjugated MOF; TEM: transmission electron microscopy; ZIF: zeolitic imidazolate framework; SALE: solvent-assisted ligand exchange.

In another study, Yu *et al.* demonstrated a solvent-assisted ligand exchange method to prepare thirteen types of MOF structures [Figure 10D][92]. During the exchange, different dimensional MOFs with weaker bonds are used as templates. The thermodynamic driving force for the ligand exchange results in the formation of more stable coordination bonds than the original ones. After dissolution and recrystallization, more stable ZIFs could be obtained. By adjusting the balance between the breaking of old bonds and the

formation of new bonds, various MOF nanostructures, such as yolk-shell nanocubes, ball-in-box nanocubes, ZIF nanotubes, and bead-on-string hybrid structures, could be obtained [Figure 10E-H].

*Other methods*

In addition to acid etching and ligand-exchange, recent research has shown that other methods such as Marangoni effect, solvent etching, and lithography can also construct intricate MOF nanostructures[93,94].

Bai *et al.* converted 3D ZIF-67 nanocubes into 2D ZIF-L nanoframes through the Marangoni effect [Figure 11A][95]. After forming the ZIF-67 nanocube, the reaction supernatant of ZIF-67 is removed, and the remaining mother liquor is transferred to the square silicon plate. Removal of the supernatant causes the concentration of Co-2-methylimidazole coordination compounds in the solution to be higher than when the system reaches thermodynamic equilibrium, triggering the growth of ZIF-L at the edges of ZIF-67 nanocuges with high surface energy. The Marangoni convection induced by the temperature gradient after the crystal is transferred to the silicon plate significantly influences the mass transfer velocity at the liquid-solid interface. The 3D ZIF-67 crystal is more prone to collapse in the water system under the attack of water molecules, which promotes the crystallization of ZIF-L and the decrystallization of ZIF-67. With the continuous transformation, the nanocube is gradually transformed into a nanoframe [Figure 11B-E].

In the MOF nanostructure transformation, the use of gas or solvent can also play a similar role to acid etching. As depicted in Figure 11F, Dutta *et al.* developed a lattice-guided wet-chemical etching strategy to synthesize 2D MOF-5 nanosheets with plus-shaped and fractal-patterned pores (*plus*-MOF and *frac*-MOF)[96]. The etching process proceeds through a two-step mechanism, where the exchange of metal-coordinating N, N-dimethylacetamide (DMAc) solvent molecule with ethanol, followed by the dissolution of the ethanol-bound Zn nodes. Since fewer BDC ligand bridges need to be broken to etch the MOF-5 crystal along the (100) direction, the energy required is relatively low, and thus, it is thermodynamically easier to obtain plus-pores etched in the (100) direction [Figure 11G]. When the etchant is reduced, the slow diffusion of the etchant is controlled by kinetics. Since solvent exchange along the (110) direction has a lower energy barrier, it is easier to obtain fractal pores etched along the (110) direction [Figure 11H].

In another study, Wei *et al.* synthesized internally tunable MOF (UiO-66) nanocages using ion etching [Figure 12A][97]. The hollow nanocages feature elongated channels with dimensions of 80-90 nm [Figure 12B-D], and they maintain high crystallinity after etching. During the etching process, the {100} facets of UiO-66, which possess higher curvature, activity, and surface energy, and larger pore sizes conducive to ion diffusion into the interior, exhibit greater reactivity. The alkaline $WO_4^{2-}$ diffuses into the MOF lattice and reacts with the acid centers Zr-oxo clusters, disrupting the metal-ligand coordination bonds in the MOF while simultaneously generating $WO_3$. The size of the internal channels of the nanocages can be finely tuned by adjusting the number of ions introduced.

To avoid etching damage and contamination, lithography techniques can also be employed to construct hierarchical MOF nanostructures. In a recent study, Tu *et al.* achieved high-quality patterned ZIF films using direct X-ray and electron-beam lithography [Figure 12E][98]. By treating halogenated ZIF-71 films with X-rays through a mask [X-ray lithography (XRL)] or direct electron-beam writing [electron-beam lithography (EBL)], halogenated ZIFs in the irradiated areas undergo decomposition. This changes the solubility of the MOF, which could then be dissolved and removed by dimethylsulfoxide (DMSO), thus obtaining hierarchical MOF structures [Figure 12F and G].

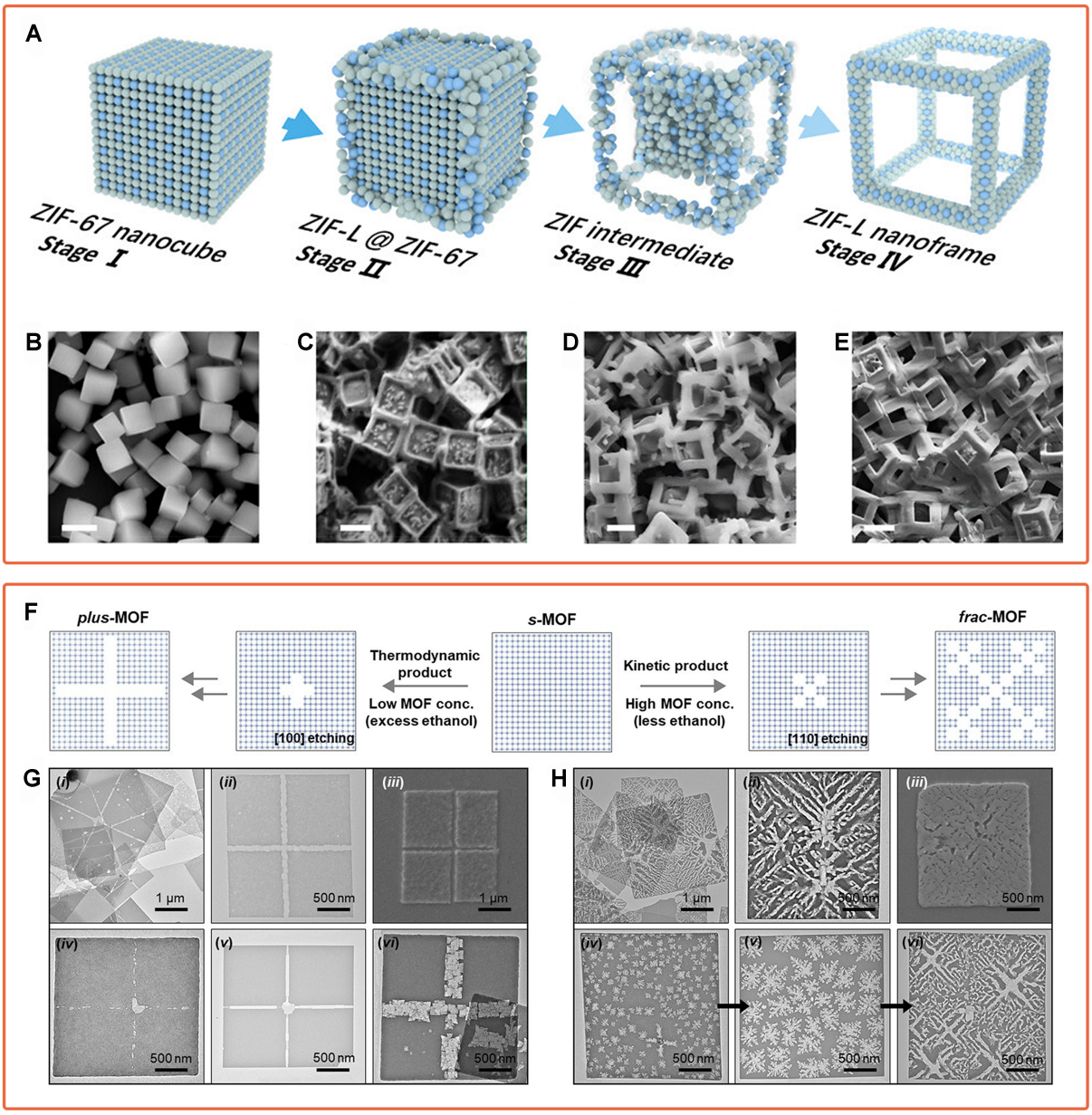


**Figure 11.** (A) Schematic illustration of the transformation process from ZIF-67 to ZIF-L; (B-E) SEM images of different transformation stages[95]. Copyright 2024, American Chemical Society; (F) Formation mechanism of two distinctly pore patterns across 2D MOF surface under altered etching conditions; SEM and TEM images of (G) *plus*-MOF and (H) *frac*-MOF[96]. Copyright 2023, Wiley-VCH. Scale bars: (B) 1 μm, (C) 1 μm, (D) 1 μm, and (E) 1 μm. ZIF: Zeolitic imidazolate framework; SEM: scanning electron microscopy; 2D: two-dimensional; MOF: metal–organic framework; TEM: transmission electron microscopy.

## CATALYTIC APPLICATIONS OF THE HIERARCHICAL MOF NANOARCHITECTURES

The construction of MOF-based nanostructures can significantly overcome the limitations of low accessibility to active sites in traditional microporous MOFs, thereby increasing their utilization efficiency and catalytic activity[99,100]. Alternatively, by purposefully integrating MOFs with different functions into heterogeneous structures, the function of MOF composite catalysts can be customized and the application range of catalysts can be expanded[77]. This section focuses on the performance enhancement brought by MOF-based nanostructures in thermal catalysis, electrocatalysis, and photocatalysis. We also summarize the relationship between diverse nanostructures and their catalytic performances.

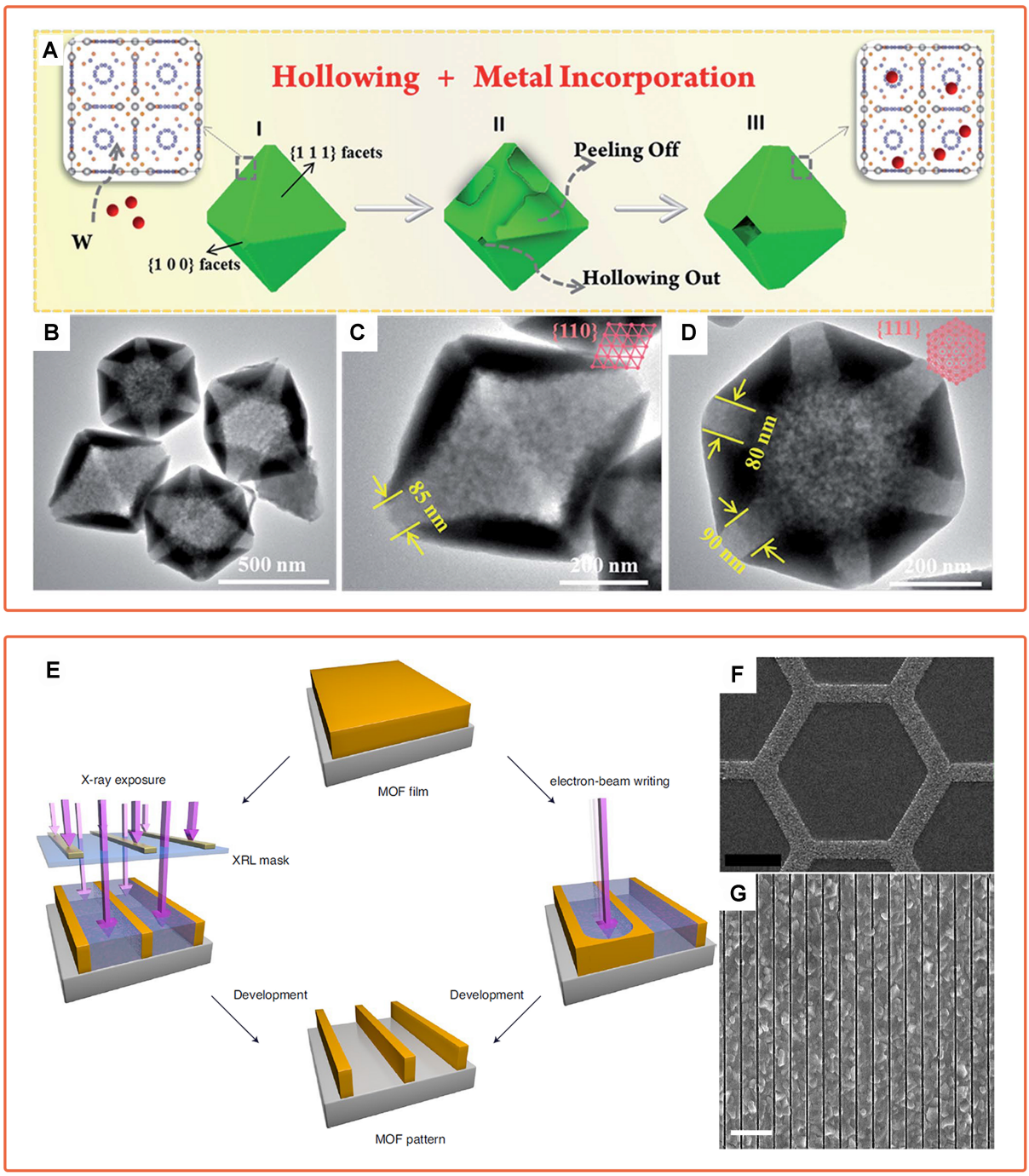


**Figure 12.** (A) Schematic illustration of the formation mechanism of W/UiO-66 nanocages; (B-D) TEM images of several W/UiO-66 nanocages observed from different directions[97]. Copyright 2018, Royal Society of Chemistry; (E) Schematic illustration of direct patterning of MOF films by XRL and EBL; (F) SEM image of ZIF-71 film after XRL patterning; (G) SEM image of ZIF-71 films after EBL patterning[98]. Copyright 2020, Springer Nature. Scale bars: (F) 20 μm and (G) 1 μm. TEM: Transmission electron microscopy; MOF: metal–organic framework; XRL: X-ray lithography; EBL: electron beam lithography; SEM: scanning electron microscopy; ZIF: zeolitic imidazolate framework.

### Thermal catalysis

Due to their unique advantages such as designable functional frameworks and adjustable pore structures, MOFs demonstrate great potential in the field of thermal catalysis[101-103]. However, as the size of reactants increases or reaction conditions (temperature, pressure, concentration, *etc.*) become milder, the performance of MOFs often falls short of expectations. Rational structural design can further enhance the performance in thermal catalysis. For example, hierarchical pores can alleviate diffusion limitations[21,104,105], and low-dimensional nanostructures can expose more active sites[106,107]. Moreover, proper MOF-on-MOF heterostructures composed of multiple functional MOFs with synergistic effects can achieve high catalytic efficiency in the complex catalytic systems requiring multi-function active sites[72].

Ai *et al.* synthesized hierarchically porous MOFs (HP-UiO-66-$NH_2$) through a "rigid modular-assisted defect formation" strategy[99]. The resulting HP-UiO-66-$NH_2$ retains octahedral morphology and exhibits mesopores in the range of 2 to 17 nm [Figure 13A]. Compared with microporous samples, the defective sites in HP-MOFs facilitate the introduction of the trifluoromethanesulfonate (OTf) group. In the synthesis of 2,3-dihydroquinazoline-4(1*H*)-one through the tandem catalysis of 2-aminobenzamide and aromatic aldehydes, the OTf group facilitates the deacetalization of benzaldehyde dimethyl acetal to benzaldehyde, allowing the reaction to proceed further to produce the final product. Due to the mass transfer advantage brought by the hierarchically porous structure, the conversion rate of tandem deacetalization-acetalization catalysis over HP-UiO-66-$NH_2$-OTf is 99%, with a selectivity of 81%, much higher than those of microporous UiO-66-$NH_2$-OTf (30% and 40%, respectively, Figure 13B). At the same time, HP-UiO-66-$NH_2$-OTf maintains high conversion rates and selectivity across multiple catalytic cycles [Figure 13C].

As the size of reactants increases, the narrow pores of MOF nanomaterials, to some extent, restrict the diffusion of reactants within the framework. The 3D hierarchical porous structures can effectively improve the mass transport of reactants, providing more accessible active sites and, thus, enhancing catalytic activity[108,109]. In a recent study, Xu *et al.* synthesized mesoporous ZIFs (mZIFs) through a polymer-micelle templating strategy [Figure 13D][110]. The hierarchical meso-/micropore structure plays a crucial role in the catalytic Knoevenagel reaction between malononitrile and benzaldehydes. As depicted in Figure 13E, under the same conditions, the mZIF-8 exhibits a faster mass transfer rate and more accessible active sites, resulting in significantly reduced reaction times compared to the conventional ZIF-8 (cZIF-8). When the reactants are replaced with a series of larger-sized molecules, mZIF-8 demonstrates higher activity in all reactions [Figure 13F].

The 2D hierarchically porous MOFs can combine the advantages of 2D nanoarchitectures and hierarchically porous materials to further improve mass transfer in catalytic reactions and expose more accessible active sites. Our group synthesized 2D UiO-66-$NH_2$ hierarchically porous nanosheets (denoted as 2D UiO-66-$NH_2$ HPNSs) through a "hard" emulsion-induced interface super-assembly strategy [Figure 13G][32]. Thanks to the thin thickness of the 2D structure and the highly open porous structure, 2D UiO-66-$NH_2$ HPNSs exhibit significantly increased yield in the cycloaddition reaction of $CO_2$ with glycidyl-2-methylphenyl ether [Figure 13H]. Compared with the other three UiO-66-$NH_2$ catalysts with different porous nanostructures, 2D UiO-66-$NH_2$ HPNSs show the highest reaction yield (96%) of cyclic carbonate product. Distinct from the UiO-66-$NH_2$ microporous crystals (MicroCs, 29%), the enhanced yields of cyclic carbonate after catalyzed by mesoporous crystals (MesoCs, 69%) and 2D microporous nanosheets (MicroNSs, 74%) further indicates that the mesoporous structure and the thin thickness can improve the accessibility of substrates to Lewis acid sites in the catalysts [Figure 13I]. Moreover, 2D UiO-66-$NH_2$ HPNSs exhibit excellent cycle stability and maintain high reaction yield after ten cycles [Figure 13J].

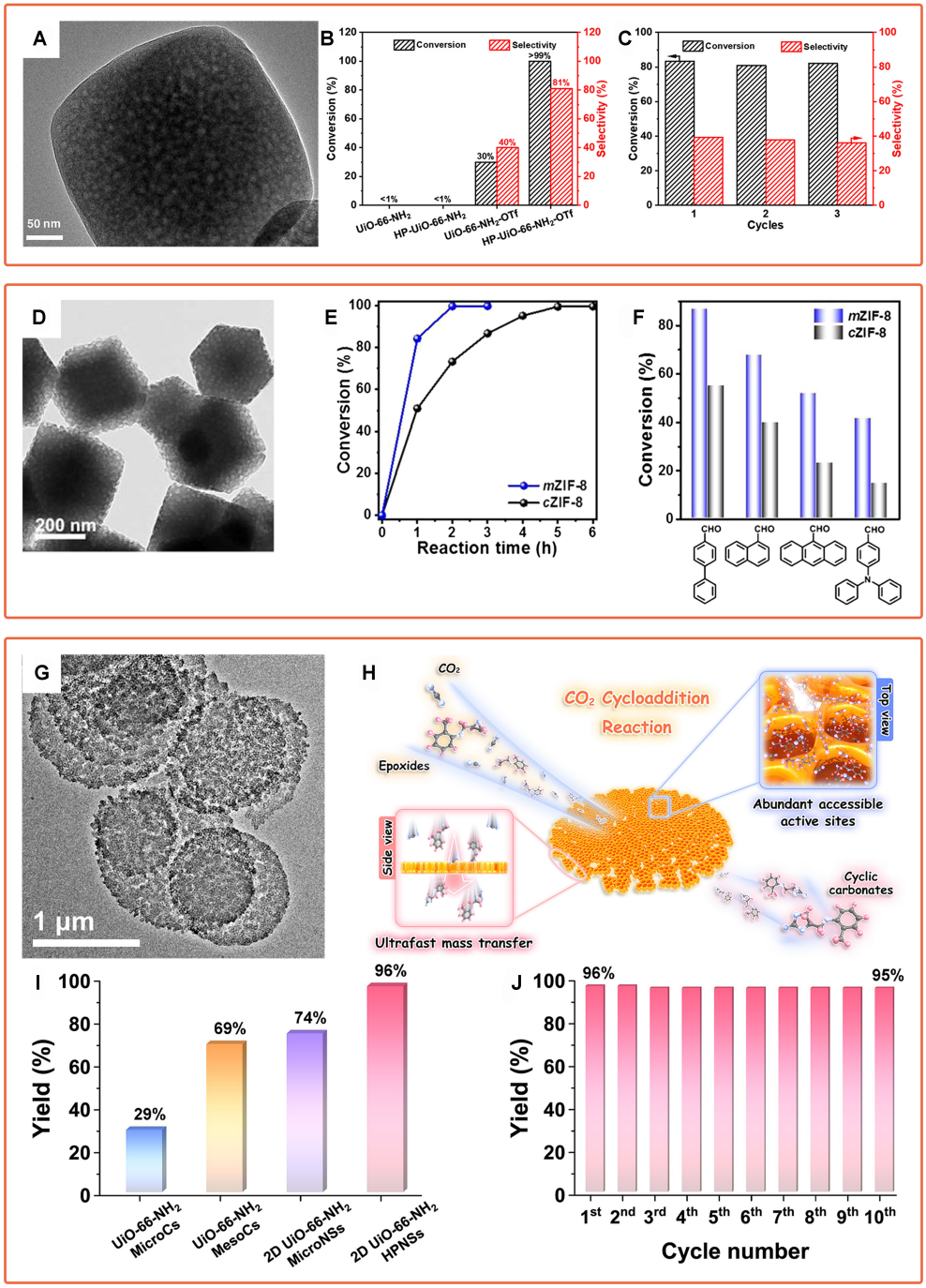


**Figure 13.** (A) TEM image of HP-UiO-66-$NH_2$; (B) Conversion of tandem deacetalization-acetalization catalysis over different catalysts; (C) Recycling test of the tandem catalysis with epibromohydrin over HP-UiO-66-$NH_2$-OTf[99].Copyright 2022, Chinese Chemical Society; (D) TEM image of mZIF-8; (E) Conversion of benzaldehyde as a function of reaction time and (F) comparison of the conversion catalyzed for various benzaldehydes by mZIF-8 or cZIF-8[110].Copyright 2021, Chinese Chemical Society; (G) TEM image of 2D UiO-66-$NH_2$ HPNSs; (H) Schematic illustration of the reaction catalyzed by a 2D UiO-66-$NH_2$ HPNS; (I) Comparison of the yields by diverse catalysts; (J) Yields of ten recycle runs using 2D UiO-66-$NH_2$ HPNS catalysts[32].Copyright 2024, American Chemical Society. TEM: Transmission electron microscopy; m-ZIF: mesoporous ZIF, ZIF: zeolitic imidazolate framework; c-ZIF: conventional ZIF; 2D: two-dimensional.

In another study, our group synthesized dendritic hierarchically porous UiO-66 nanoparticles (DHPNPs-x, where x represents the reaction temperature) constructed from a continuous bent 2D sheet via noncentrosymmetric pore-induced anisotropic assembly [Figure 14A][57]. In a model reaction involving the cycloaddition of $CO_2$ and epoxides, the highly open dendritic structure provides abundant Lewis acidic sites for catalytic reactions, facilitating the ring-opening of epoxides and subsequent transformations. Compared to the microporous UiO-66 (67.9%), the yield of cyclic carbonate products over MOF catalysts with dendritic hierarchical pore structures significantly increases. With an increase in the average pore diameter of DHPNPs from 35 nm (DHPNPs-30) to 100 nm (DHPNPs-45), the reaction yield increases from 91.9% to 97.4%, further demonstrating that the open pore structure enhances mass transfer and reaction kinetics [Figure 14B and C].

Compared with hierarchically porous structures, mesoporous hollow multi-shell structures can enrich reactants while maintaining an excellent mass transfer rate, thereby enhancing catalytic performance. As mentioned, our research group synthesized nS-mesoUiO-66-$NH_2$ HoMSs using a dual-template-directed successive assembly strategy [Figure 14D and E][22]. When methylene blue is used as the model molecule, the mesoporous hollow multi-shell structure shows faster adsorption kinetics and higher adsorption capacity with the increase of MOF nanoshells [Figure 14F]. Due to their capability to enrich organic molecules and abundant Lewis acidic sites in their MOF framework, 3S-mesoUiO-66-$NH_2$ HoMSs exhibit higher catalytic activity than microporous UiO-66-$NH_2$ when cycloaddition reaction of epoxide and carbon dioxide is used as the probe reaction, and the conversion rate of 2-methylphenyl ether reaches 95% at 10 h. In addition, the catalytic yield of cyclic carbonate product increases with the nanoshells in nS-mesoUiO-66-$NH_2$ HoMSs [Figure 14G]. The excellent catalytic activity of 3S-mesoUiO-66-$NH_2$ HoMSs may be attributed to the enrichment of organic reactants by mesoporous multi-shell hollow structure, which enhances catalytic reaction kinetics [Figure 14H].

Constructing rational nanostructures not only enhances catalytic efficiency but also improves the selectivity of catalytic reactions[111]. By changing the diffusion rate of the substrate in the nanostructure, the residence time of the reactants in the skeleton could be controlled, thus improving the yield and selectivity of the catalytic reaction. As illustrated in Figure 15A, Qin *et al.* synthesized the hollow mesoporous structure MIL-101 (HM-MIL) by selective etching of solid Cr, Al-bimetallic MIL-101 (S-MIL)[85]. By simulating the effect of nanostructures on the diffusion rate of 4-chlorostyrene, it is found that the diffusion rate of the substrate in HM-MIL is significantly faster than that in S-MIL, owing to the larger porosity and wider channels of HM-MIL. This also results in superior catalytic activity of HM-MIL compared to both S-MIL and hollow MIL-101 (H-MIL) in the catalysis of 4-chlorostyrene oxidation. Importantly, the selectivity of the reaction exhibits a similar trend, attributed to the rapid diffusion of the oxidation product epoxide, thus avoiding further oxidation of epoxides into aldehydes within the MOF micropores [Figure 15B and C].

The selectivity of catalytic products can be completely switched by changing the nanostructure of the catalysts and the content of active sites simultaneously. In another study, He *et al.* synthesized yolk-shell structures (YSS-n, where n indicates the serial number of the sample with different Ce/Zr ratios) with UiO-66(Ce) as the yolk and UiO-66(Zr) as the shell through a cluster stabilization strategy. Subsequently, they prepared single-shell hollow structures (SSHS-n, where n indicates the serial number of the sample with distinct Ce/Zr ratios) by a post acid treatment [Figure 15D-G][25]. When using the formation of quinazolinone analogs as a model reaction, differences in catalytic activity of the catalyst can affect the degree of the reaction. The reaction of benzaldehyde with o-aminobenzamide can produce imine, and 2,3-dihydroquinazolinone can be further generated with the increase of the reaction degree. Notably, when SSHS is used as the catalyst, the product is only imide, and the catalytic performance gradually decreases as the $Ce^{IV}$ content increases. In contrast, when YSS is used as the catalyst, the product is exclusively

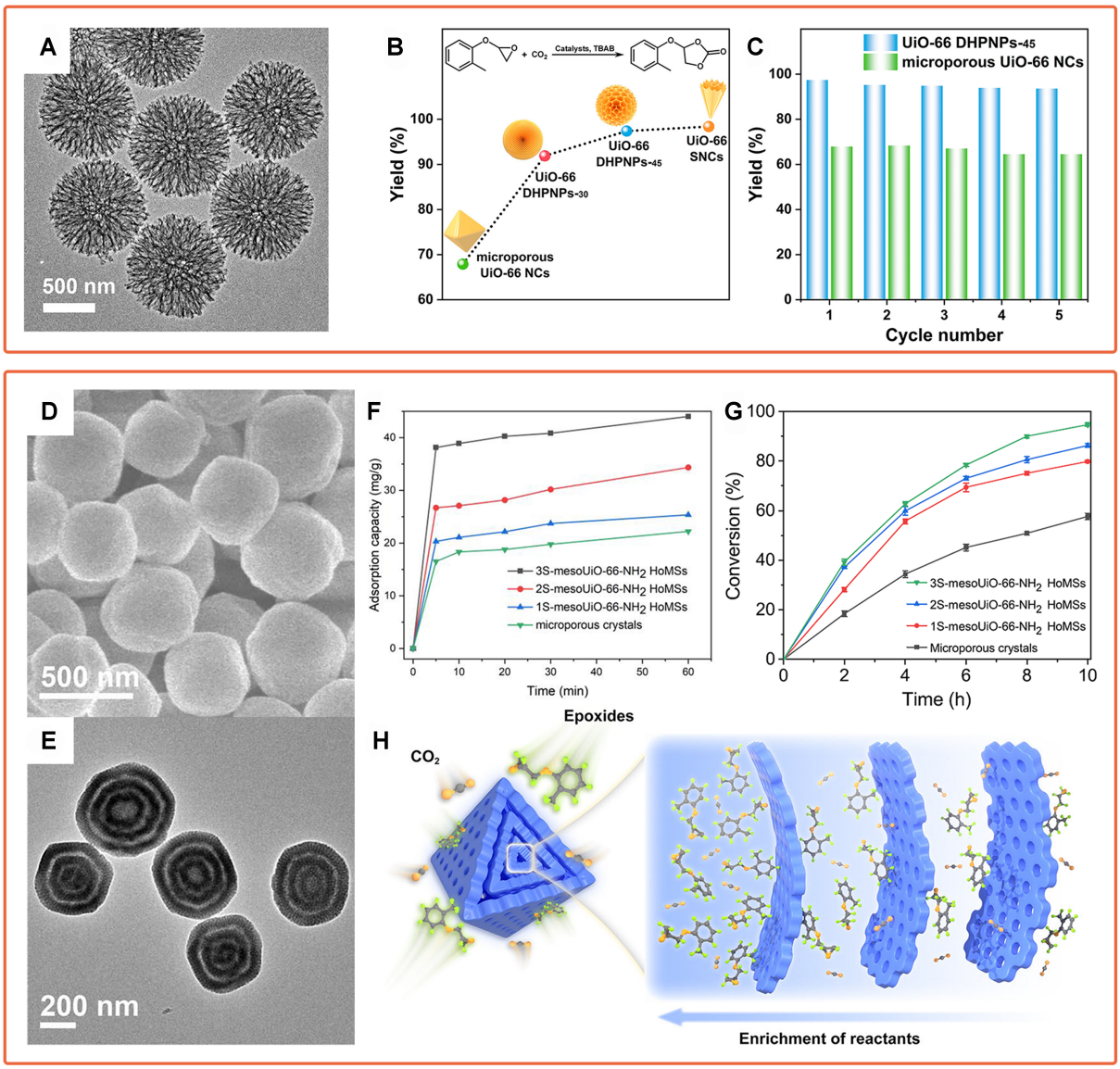


**Figure 14.** (A) TEM image of UiO-66 DHPNPs; (B) Kinetic profile for the $CO_2$ cycloaddition reaction using different catalysts; (C) Yields of five recycle runs using UiO-66 DHPNPs-$_{45}$ and microporous NCs as catalysts[57]. Copyright 2023, American Chemical Society; (D) SEM and (E) TEM images of 3S-mesoUiO-66-$NH_2$ HoMSs; (F) Adsorption capacity of 3S-mesoUiO-66-$NH_2$ HoMSs, 2S-mesoUiO-66-$NH_2$ HoMSs, 1S-mesoUiO-66-$NH_2$ HoMSs, and microporous crystals at varying contact times; (G) Comparison of the conversion catalyzed for catalytic cycloaddition reactions between $CO_2$ and glycidyl-2-methylphenyl ether by multiple catalysts; (H) Schematic illustration of reactant enrichment in a 3S-mesoUiO-66-$NH_2$ HoMS[22]. Copyright 2023, Springer Nature. TEM: Transmission electron microscopy; DHPNPs: hierarchically porous MOF (UiO-66) nanoparticles; NCs: nanocrystals; SEM: scanning electron microscopy.

dihydroquinazolinone, and the yield increases with the $Ce^{IV}$ content [Figure 15H]. Through simulations and mechanistic studies, it was found that defects in SSHS-2 can significantly improve molecular diffusion so that the product imine molecules can easily enter the interior of the framework. YSS-2, with a slower adsorption and desorption rate, has a longer retention time for the reaction substrate, and the content of $Ce^{IV}$ with high redox activity in YSS-2 is much higher than that of SSHS-2. Therefore, YSS will catalyze the reaction to generate 2,3-dihydroquinazolinone with a higher reaction degree. The reaction products of SSHS with faster diffusion rate and fewer $Ce^{IV}$ sites are mainly imines.

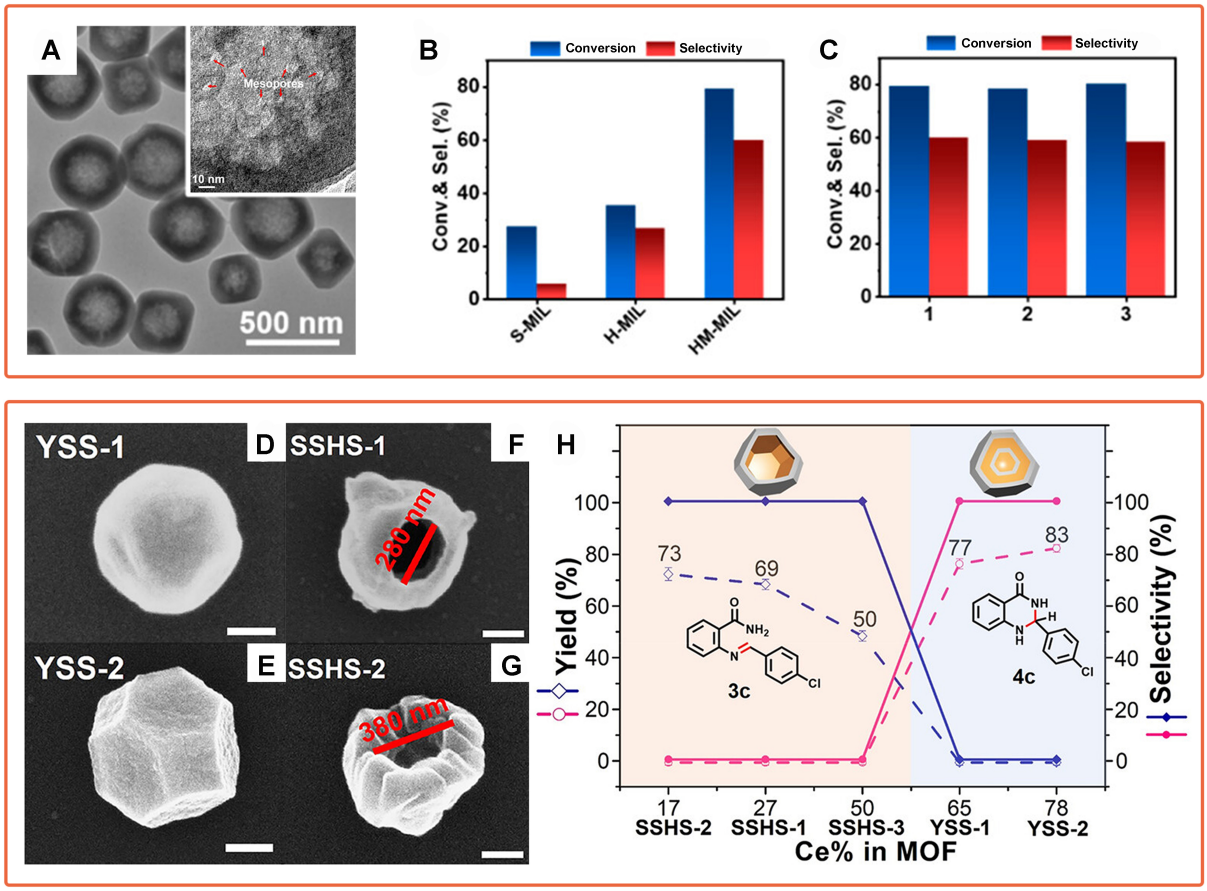


**Figure 15.** (A) TEM image of HM-MIL; (B) Catalysis properties of S-MIL, H-MIL, and HM-MIL and (C) recycle runs of HM-MIL on 4-chlorostyrene oxidation[85]. Copyright 2020, American Chemical Society; (D-G) SEM images of (D) YSS-1, (E) YSS-2, (F) SSHS-1, and (G) SSHS-2; (H) Yield and selectivity of the reaction of 4-chlorobenzaldehyde and o-aminobenzamide[25]. Copyright 2023, American Chemical Society. Scale bars: (D) 200 nm, (E) 200 nm, (F) 200 nm, and (G) 200 nm. TEM: Transmission electron microscopy; MIL: Materials Institute Lavoisier; SEM: scanning electron microscopy; YSS: yolk-shell structures; SSHS: single-shell hollow structures.

## Electrocatalysis

In recent years, increasing exploration has been into renewable energy sources to replace traditional fossil fuels. Among these efforts, research on electrocatalysis has garnered significant attention[112-116]. The activity of electrocatalysis increases with the area involved in electron transfer (electrochemically active area). MOFs possess large specific surface areas, high porosity, and a high proportion of metals, which endow them with a high density of active sites, so they can be considered as potential electrocatalysts[42,117]. Furthermore, rational design and construction of suitable MOF nanostructures can further enhance their structural advantages and improve electrocatalytic performances[118].

As an example, Ge *et al.* utilized a small amount of water and triethylamine (TEA) to synthesize bimetallic MOF (MOF-Fe/Co) nanosheets on a large scale [Figure 16A][119]. The TEA could not only deprotonate carboxylic acids to accelerate coordination polymerization but also interact with water to produce $OH^-$ to stabilize the edges of 2D MOF layers and inhibit the formation of 3D structures. The 2D MOF-Fe/Co has a thickness of 2.2 nm and lateral dimensions ranging from 300 to 500 nm. As shown in Figure 16B, compared with bulk MOF-Fe/Co (427 mV) and 3D MOF-Fe/Co (311 mV), the 2D MOF-Fe/Co exhibits the lowest overpotential (238 mV) at a current density of 10 $mA \cdot cm^{-2}$ in the oxygen evolution reaction (OER) under alkaline conditions. Moreover, the Tafel plots demonstrate that the 2D MOF-Fe/Co had the most efficient

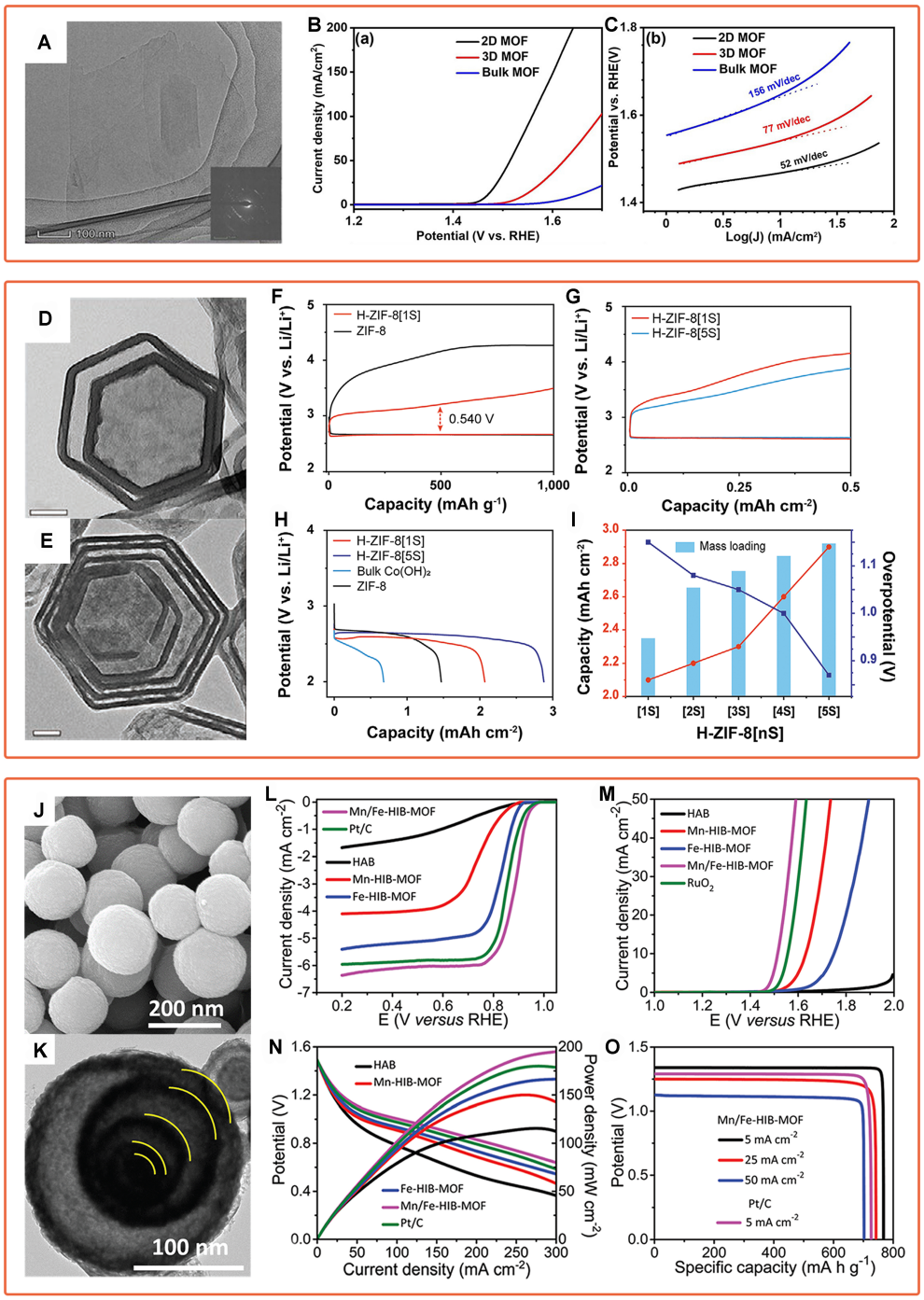


**Figure 16.** (A) TEM image of 2D MOF-Fe/Co; (B and C) Electrochemical performances of the MOF-Fe/Co with various shapes on OER. (B) iR-corrected polarization curves and (C) corresponding Tafel plots derived from the LSV curves[119]. Copyright 2021, Wiley-VCH; (D and E) TEM image of (D) H-ZIF-8[2S] and (E) H-ZIF-8[5S]; (F) Gravimetric discharge and charge curves of H-ZIF-8[1S] and ZIF-8 at a current density of 50 mA·g$^{-1}$ with a cutoff capacity of 1,000 mAh·g$^{-1}$; (G) Geometric discharge and charge curves of H-ZIF-8[1S] and H-ZIF-8[5S] at a constant current of 0.1 mA·cm$^{-2}$ with a cutoff capacity of 0.5 mAh·cm$^{-2}$; (H) Full geometric discharge curves at a constant current density of 0.1 mA·cm$^{-2}$; (I) Comparison plot of capacity and overpotential according to mass loading[120]. Copyright 2020, Wiley-VCH; (J) SEM and (K) TEM images of Mn/Fe-HIB-MOF; (L) ORR and (M) OER polarization profiles of the different catalysts; (N) Discharging and power density profiles for primary ZABs for the M-HIB-MOFs; (O) Discharge plots of ZABs for Mn/Fe-HIB-MOF air cathodes for distinct current densities[121]. Copyright 2019, Royal Society of Chemistry. Scale bars: (D) 50 nm and (E) 50 nm. TEM: Transmission electron microscopy; 2D: two-dimensional; MOF: metal–organic framework; OER: oxygen evolution reaction; LSV: linear sweep voltammetry; ZIF: zeolitic imidazolate framework; SEM: scanning electron microscopy; ORR: oxygen reduction reaction; ZAB: Zn–air battery.

catalytic kinetics [Figure 16C]. Compared to 3D structures, the 2D structure promotes charge transfer on the material surface and exposes more active sites, resulting in higher conductivity and OER activity.

In addition to 2D structures, some intricate 3D structures can also significantly reduce transport resistance and promote improvements in electrocatalytic performance. In a recent study, Choi *et al.* obtained multilayer hollow ZIF-8 (H-ZIF-8 [nS], where n is the number of shells) by alternately stacking multilayered water-stable MOF (ZIF-8) and water-decomposable MOF (ZIF-67)[120], using the hydrogen bonding affinity between ethylene glycol (EG) and water to shrink water clusters, allowing them to pass through the pores of ZIF-8, and the incoming water selectively decomposes the unstable MOF layer. Through repeated epitaxial growth, the number of layers of multi-shell MOFs can be increased from two to five [Figure 16D and E]. The decomposed ZIF-67 layers transition into stable dinuclear $Co(OH)_2$ sub-nanometric particles (SNPs) loaded within the multilayered structure. When the material is used as an electrocatalyst in lithium-oxygen batteries, the presence of SNPs significantly reduces the overpotential of OER during the charging process. Meanwhile, the hollow structure provides a large surface area for electrocatalysis, reducing transport resistance and, thus, enhancing electrochemical performance [Figure 16F-H]. Additionally, with more layers of H-ZIF-8 [nS], the mass loading rises, resulting in a gradual enhancement in capacity and a reduction in overpotential [Figure 16I].

In another study, Shinde *et al.* demonstrated a novel 3D dual-linked hexaiminobenzene MOF (Mn/Fe-HIB-MOF)[121]. The MOF particles possess a structure resembling a quintet-shells hollow sphere and an extremely high surface area (2,298 $m^2 \cdot g^{-1}$), providing active sites and rapid electron/mass transfer pathways for electrocatalysis [Figure 16J and K]. Compared to Pt/C and single-metal MOFs, Mn/Fe-HIB-MOF exhibits the highest onset potential (0.98 V), most positive half-wave potential (0.883 V), and smallest Tafel slope (36 $mV \cdot dec^{-1}$) in the oxygen reduction reaction (ORR) under alkaline conditions [Figure 16L]. Additionally, as illustrated in Figure 16M, Mn/Fe-HIB-MOF shows excellent OER performance (overpotential of 280 mV at a current density of 10 $mA \cdot cm^{-2}$). In zinc-air batteries with Mn/Fe-HIB-MOF as the electrode, a power density of 195 $mW \cdot cm^{-2}$ is achieved, and the specific capacity is 769 $mA \cdot h \cdot g^{-1}$ at a current density of 5 $mA \cdot cm^{-2}$ [Figure 16N and O].

### Photocatalysis

Photocatalysis is an efficient, safe, and environmentally friendly technology that converts solar energy into other types of chemical energy[122]. In recent years, MOFs with abundant carrier charge transfer pathways and active sites have been considered as novel and efficient photocatalysts[123-126]. Compared to other types of catalysts, MOFs not only exhibit controllable composition but also have more easily adjustable nanostructures. By altering the nanostructure, they can effectively provide more abundant light absorption sites, demonstrating stronger photocatalytic performance[28,127-131].

By changing the MOF morphology and adjusting the exposure ratio of the specific crystal surfaces in the photocatalytic reaction, the utilization rate of the photoexcited electron active sites can be enhanced, improving photocatalytic performance. Cheng *et al.* synthesized $HN_2$-MIL-125 ($NM_n$, where n is the dominant facet) with different {001} and {111} facet ratios, resulting in morphologies of the disk, octahedron, and truncated octahedron, respectively, to study the facet-dependent in photocatalysis [Figure 17A-D][132]. In the photocatalytic carbon dioxide reduction, the catalytic activity is enhanced with increasing the exposure ratio of {111} facets. $NM_{111}$ whose surface is dominated by {111} facets shows the highest CO and $CH_4$ yields (8.25 and 1.01 $\mu mol \cdot g^{-1} \cdot h^{-1}$), much higher than $NM_{001}$ whose surface is dominated by {001} facets [Figure 17E and F]. This is because the {111} facet in MOF exposes more Ti-$O_x$ cluster active

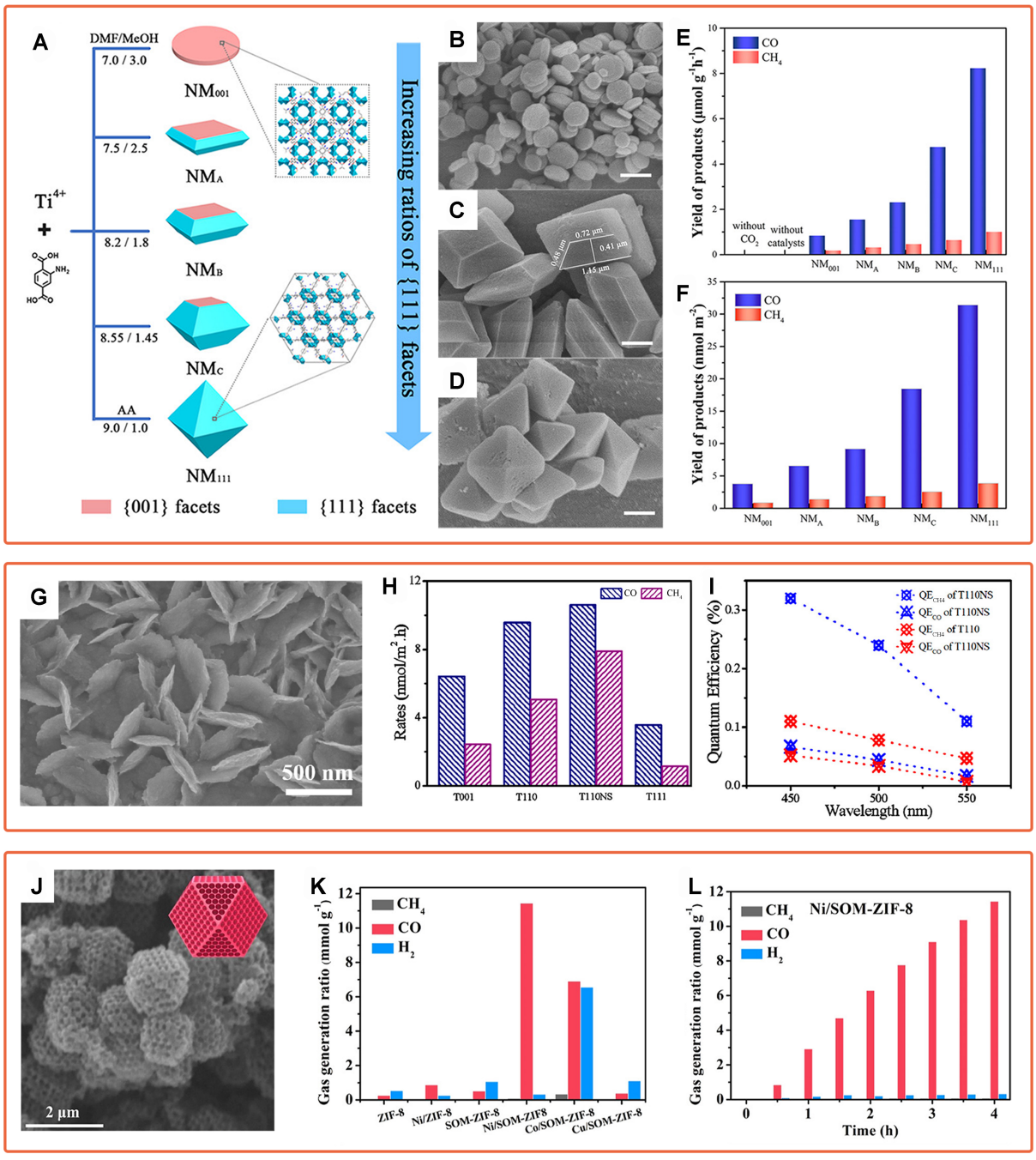


**Figure 17.** (A) Schematic illustration of the evolution of morphology and facet over $NH_2$-MIL-125(Ti) ($NM_A$, $NM_B$, and $NM_C$, where A, B, and C represent the different ratios of mixed {001} and {111} facets); (B-D) SEM images of (B) $NM_{001}$, (C) $NM_B$, and (D) $NM_{111}$; (E and F) Yields of products with respect to (E) the mass and (F) the facet surface area of catalysts[132]. Copyright 2021, American Chemical Society; (G) SEM image of ultrathin nanosheets $NH_2$-MIL-125; Comparison of (H) photocatalytic reaction rates normalized by the surface area for varied catalysts; (I) QE values of $CO_2$ photoreduction to $CH_4$ and CO[133]. Copyright 2022, American Chemical Society; (J) SEM image of Ni/SOM-ZIF-8; (K) Photocatalytic $CO_2$ reduction performance of ZIF-8, Ni/ZIF-8, SOM-ZIF-8, Ni/SOM-ZIF-8, Co/SOM-ZIF-8, and Cu/SOM-ZIF-8; (L) Histogram of the cumulative production of CO, $CH_4$, and $H_2$ over time for Ni/SOM-ZIF-8[134]. Copyright 2023, American Chemical Society. Scale bars: (B) 500 nm, (C) 500 nm, and (D) 500 nm. MIL: Materials Institute Lavoisier; SEM: scanning electron microscopy; QE: quantum efficiency; ZIF: zeolitic imidazolate framework.

sites {001} facet. In another study, Guo *et al.* synthesized ultrathin 2D MOF (MIL-125) nanosheets for photocatalytic carbon dioxide reduction[133]. The $NH_2$-MIL-125 nanosheets (T110NS) exhibit a smooth petaloid structure with a thickness of approximately 12 nm and {110} facets containing larger proportions of metal clusters [Figure 17G]. When using triethanolamine (TEOA) as a sacrificial agent for photocatalytic carbon dioxide reduction, T110NS can convert $CO_2$ into CO and $CH_4$. Additionally, it exhibits the best photocatalytic activity compared to other morphologies of $NH_2$-MIL-125 [Figure 17H and I]. density functional theory (DFT) calculations suggest that the {110} facets in 2D MOF nanosheets have more photoexcited electron Ti sites than their 3D MOF counterparts, thereby enhancing the reduction efficiency of carbon dioxide.

In addition to utilizing 2D structures to provide more exposed active sites, rationally designed 3D porous structures can also achieve rapid mass transport and gas adsorption and enhanced photocatalytic activity. In a recent study, Liu *et al.* synthesized 3D ordered macroporous structure of Ni single-atom-immobilized ZIF-8 (Ni/SOM-ZIF-8) using highly ordered 3D PS monoliths as templates [Figure 17J][134]. Benefiting from the macroporous structure and Ni single atoms, Ni/SOM-ZIF-8 exhibits excellent $CO_2$ adsorption capacity. Compared with ZIF-8 (0.26 mmol/g at 4 h) and SOM-ZIF-8 (0.51 mmol/g at 4 h) samples without Ni active sites, Ni/SOM-ZIF-8 significantly improves the CO yield of 11.44 mmol/g at four hours in photocatalytic carbon dioxide reduction. Furthermore, the CO generation rate of Ni/SOM-ZIF-8 is 13.15 times higher than that of Ni/ZIF-8 (0.87 mmol/g at 4 h), indicating that the 3D ordered macroporous structure can expose more single-atom active sites and accelerate carbon dioxide diffusion [Figure 17K and L].

Compared with polycrystalline catalysts, single-crystalline catalysts possess unique advantages in photocatalytic reactions. Zhao *et al.* synthesized hollow mesoporous MOF single crystals [HMS UiO-66(Ce)] by kinetically mediated micelle assembly strategy [Figure 18A][66]. When using $Na_2SO_3$ and $Na_2S$ as sacrificial agents, HMS UiO-66(Ce) shows superior performance in photocatalytic hydrogen evolution (PHE). Compared with hollow mesoporous polycrystalline samples [HM UiO-66(Ce), 450 μmol/g at 3 h] and solid mesoporous polycrystals UiO-66(Ce) (313 μmol/g at 3 h), HMS UiO-66(Ce) shows much higher hydrogen evolution yield (819 μmol/g at 3 h, Figure 18B). At the same time, HMS UiO-66(Ce) exhibits the strongest photocurrent response, indicating the fastest interfacial charge transfer [Figure 18C]. The hollow structure eliminates the barrier between different mesoporous channels, increasing the accessibility of active sites and improving mass transfer. In addition, compared with polycrystalline samples with more defects, the single-crystalline skeleton can not only improve the structural stability but also prevent photoinduced charge recombination, so as to obtain higher photocurrent and good cyclic stability [Figure 18D].

Rationally combining two MOFs with different functionalities makes it possible to achieve adsorption enrichment of reactants and significant enhancement in catalytic efficiency. As an example, Liu *et al.* demonstrated a site-specific epitaxial-growth strategy to grow ZIF-8 epitaxially on the {110} surfaces of cake-like and box-like MIL-125 (named $_c$MIL-125@ZIF-8 and $_b$MIL-125@ZIF-8, Figure 18E and F)[135]. In the photocatalytic degradation of dye pollutant orange II, the positively charged ZIF-8 can adsorb and enrich negatively charged dye molecules through electrostatic interaction [Figure 18G]. Therefore, in further photocatalysis, the two MIL-125@ZIF-8 composites exhibit excellent degradation efficiency (97.3% and 86.0%, respectively), much higher than that of individual MIL-125 ($_c$MIL-125: 54.6%, $_b$MIL-125: 57.3%) and ZIF-8 (8.4%). Importantly, the degradation efficiency of MIL-125@ZIF-8 is significantly higher than that of a mixture of MIL-125 and ZIF-8 in the same proportion, indicating that the heterostructures with complementary properties formed by direct contact can significantly enhance catalytic performance [Figure 18H].

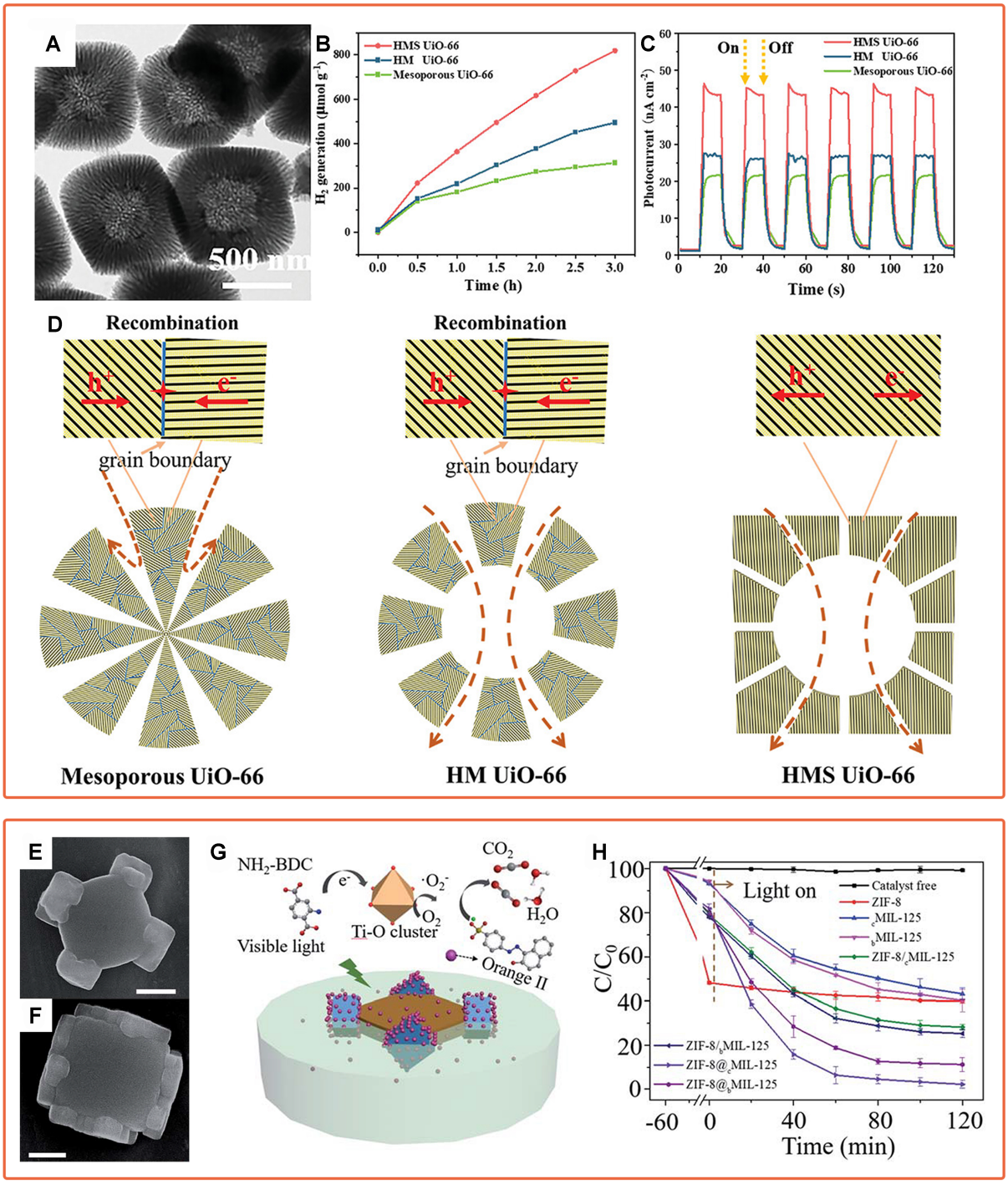


**Figure 18.** (A) TEM image of HMS UiO-66(Ce); (B) Water-splitting $H_2$ generation profiles and (C) photocurrent responses of HMS UiO-66(Ce), HM UiO-66(Ce), and solid mesoporous UiO-66(Ce); (D) Schematic illustration of the mass transfer and carrier transport processes in three samples[66]. Copyright 2023, Wiley-VCH; (E and F) SEM images of (E) $_c$MIL-125@ZIF-8 and (F) $_b$MIL-125@ZIF-8; (G) Schematic illustration of the photocatalytic degradation process towards orange II using ZIF-8@MIL-125; (H) Degradation efficiency of different catalysts[135]. Copyright 2020, Royal Society of Chemistry. Scale bars: (E) 200 nm and (F) 200 nm. TEM: Transmission electron microscopy; SEM: scanning electron microscopy; MIL: Materials Institute Lavoisier; ZIF: zeolitic imidazolate framework.

## CONCLUSION AND PERSPECTIVE

The rapidly advancing hierarchical MOF nanoarchitectures hold promising applications in heterogeneous catalysis. This review analyzes the formation mechanisms of various structural features observed in recently developed hierarchical MOF nanostructures. It outlines the methods of introducing novel pores and nanostructures into traditional MOF materials through bottom-up and top-down ways. Furthermore, it examines the structure-performance relationships of these materials across various catalytic reactions. Compared with traditional MOF materials, these novel structures reduce the diffusion limit by introducing secondary nanopores, shorten the diffusion distance by constructing the low-dimensional nanoarchitectures, and expand the application range of the catalysts by selectively integrating MOFs with different functions into heterogeneous structures, thus achieving high activity and multi-function of the catalysts. Although researchers have made significant advances in the construction and catalytic applications of hierarchical MOF nanostructures in recent years, some challenges persist to be addressed.

Further precise control over the structure and composition of MOFs remains challenging. In the design and construction of MOF nanostructures, accurately controlling pore structure and dimension is an unavoidable problem. In order to improve the controllability of MOF nanostructures, a deeper understanding of the underlying mechanisms of their formation processes is urgently needed. For instance, the latest advancements based on noncentrosymmetric pore-induced anisotropic assembly in MOFs can provide new insights into constructing complex structures of hierarchically porous MOFs with asymmetric and open architectures[57]. Such asymmetric open pore structure may provide different catalytic centers for the catalytic reaction while maintaining the mass transfer advantage of the open pore, thus achieving efficient heterogeneous catalysis. The exploration of multicomponent heterogeneous structures formed by multi-component MOFs is not deep enough. At present, constructing existing MOF-on-MOF heterostructures usually depends on the similarity of host-guest MOF topologies and lattice parameters. When the lattice constants of the two MOFs differ too much, the epitaxial growth cannot happen. Therefore, combining the lattice-mismatched host-guest MOFs is still a significant challenge. This will further extend the existing MOF-on-MOF system and take advantage of synergies between multiple components to compensate for or inhibit the limitations of individual MOFs in catalytic reactions.

It is also important to study the formation process and mechanism of hierarchical MOF nanostructures using *in situ* imaging techniques. Existing mechanistic studies often rely on investigating the influence of reaction time, temperature, reactant amounts, *etc.*, on the final nanostructure. However, there is still a lack of an intuitive understanding of the formation process of MOF-based nanostructures across various scales. At present, *in situ* transmission electron microscopy (TEM) has provided considerable convenience for the direct spatiotemporal observation of MOF dynamics and has enabled further understanding of the mechanisms of formation, growth and phase transition[136]. Therefore, using *in situ* imaging techniques to visualize the growth process of nanostructures to study the nucleation and crystallization process of MOFs, and to understand the mechanism of structure-directing agents on pore and nanostructures will provide fresh ideas for the design and synthesis of MOFs with novel and distinctive structures.

Although the hierarchical MOF nanostructures provide a shorter diffusion path and better catalytic performance for the catalytic reactions, some shortcomings cannot be ignored. (i) Stability reduction is a notable concern. For instance, incorporating hierarchical meso-/macropores in MOFs inevitably introduces defects into their intrinsic micropore structures and reduces their stability, making it difficult to maintain high cyclic stability in thermal catalysis. To address this issue, it is reasonable to construct MOF-on-MOF structures by growing a protective, stable microporous MOF layer on the surface of pore walls in hierarchical MOFs; (ii) Limitation of MOF types persists. Currently, the predominant exploration of hierarchical nanostructures focuses on several common MOFs such as UiO-66, ZIF-8 and MIL-101, but

their electrical conductivity or light absorption capacity needs to be improved. Therefore, directing attention towards synthesizing more functional MOFs in future exploration is imperative, which will significantly expand their application in electro-/photocatalysis; (iii) The product selectivity is constrained. Typically, the construction of hierarchical MOF nanostructures solely improves the yield of catalytic reactions without affecting the product selectivity. At present, machine learning has significantly contributed to developing and applying MOFs, assisting in predicting the selective adsorption of gases and the accessibility of guests[137,138]. Using it to compute and screen materials in advance offers rational approaches to avoid a large number of trial-and-error experiments, facilitating the discovery of materials with high product selectivity; (iv) The structure-performance relationship is unclear. There is no intuitive way to express the improvement degree of hierarchical nanostructure on performance in catalytic reaction. The relationship between hierarchical nanostructure and performance requires a visual numerical representation, for example, by building a suitable model to assess the utilization efficiency of the overall structure in catalysis; (v) The theoretical calculations pose significant challenges, particularly in the simulation scale of DFT commonly used in catalysis, which often diverges from the actual scale of hierarchical MOF nanostructures. So, the simulations often fail to capture the complexity of actual hierarchical MOF nanostructures, leaving both the construction and accuracy of the models unresolved. Moreover, ingenious calculation methods may provide new ideas for theoretical calculations in catalytic reactions. For example, finite element analysis (FEA) can be used to calculate the degree of the reactant enrichment within the hierarchical nanostructures in the catalytic system, which can prove the advantages of the hierarchical nanostructure to the performance enhancement.

Expanding synthetic methods to large-scale production levels is also a challenge. In large-scale production, it is necessary to balance the economic costs and environmental impacts associated with synthesis. At present, the synthesis of hierarchical nanostructured MOFs often entails high costs and pollution in various aspects. In terms of cost, achieving various structures requires additional materials, such as templates and etchants, in the synthesis process. Additionally, using various functionalized organic ligands and metals implies higher costs. In terms of the environment, removing templates and washing raw materials requires various organic solvents, and the increase in organic waste undoubtedly has a greater impact on the environment. Therefore, it is necessary to explore economically friendly and green synthesis routes, such as recycling raw materials from waste solutions or using solvent-free synthesis methods.

Despite facing numerous challenges, it is foreseeable that MOFs will continue to play a crucial role in chemistry, materials, and other related fields. As an important part of MOF synthesis, constructing their hierarchical nanostructures is expected to play an irreplaceable role in improving catalytic performance. This review highlights advances in hierarchical MOF nanostructures and our views on the challenges and opportunities. This field is anticipated to achieve exciting progress with the joint efforts of all.

## DECLARATIONS

### Authors' contributions

Prepared the manuscript: Zhao B, Han J, Liu B
Performed manuscript correcting: Zhang SL, Guan B

### Availability of data and materials

Not applicable.

### Financial support and sponsorship

This work was supported by the National Natural Science Foundation of China (Grant 22375071, 22288101, and 21920102005), National Key Research and Development Program of China (Grant 2021YFA1501202

and 2022YFA1503600), and the "111 Center" (B17020).

### Conflicts of interest

All authors declared that there are no conflicts of interest.

### Ethical approval and consent to participate

Not applicable.

### Consent for publication

Not applicable.

### Copyright



## REFERENCES

1. Deng H, Doonan CJ, Furukawa H, et al. Multiple functional groups of varying ratios in metal-organic frameworks. *Science* 2010;327:846-50. DOI PubMed
2. Li H, Eddaoudi M, O'keeffe M, Yaghi OM. Design and synthesis of an exceptionally stable and highly porous metal-organic framework. *Nature* 1999;402:276-9. DOI
3. Furukawa H, Cordova KE, O'Keeffe M, Yaghi OM. The chemistry and applications of metal-organic frameworks. *Science* 2013;341:1230444. DOI PubMed
4. Bavykina A, Kolobov N, Khan IS, Bau JA, Ramirez A, Gascon J. Metal-organic frameworks in heterogeneous catalysis: recent progress, new trends, and future perspectives. *Chem Rev* 2020;120:8468-535. DOI PubMed
5. Chen L, Xu Q. Metal-organic framework composites for catalysis. *Matter* 2019;1:57-89. DOI
6. Corma A, García H, Llabrés i Xamena FX. Engineering metal organic frameworks for heterogeneous catalysis. *Chem Rev* 2010;110:4606-55. DOI PubMed
7. Pascanu V, González Miera G, Inge AK, Martín-Matute B. Metal-organic frameworks as catalysts for organic synthesis: a critical perspective. *J Am Chem Soc* 2019;141:7223-34. DOI PubMed
8. Lu W, Wei Z, Gu ZY, et al. Tuning the structure and function of metal-organic frameworks via linker design. *Chem Soc Rev* 2014;43:5561-93. DOI PubMed
9. Cai G, Yan P, Zhang L, Zhou HC, Jiang HL. Metal-organic framework-based hierarchically porous materials: synthesis and applications. *Chem Rev* 2021;121:12278-326. DOI PubMed
10. Chai L, Pan J, Hu Y, Qian J, Hong M. Rational design and growth of MOF-on-MOF heterostructures. *Small* 2021;17:e2100607. DOI PubMed
11. Zhao Z, Ding J, Zhu R, Pang H. The synthesis and electrochemical applications of core–shell MOFs and their derivatives. *J Mater Chem A* 2019;7:15519-40. DOI
12. Xiao X, Zou L, Pang H, Xu Q. Synthesis of micro/nanoscaled metal-organic frameworks and their direct electrochemical applications. *Chem Soc Rev* 2020;49:301-31. DOI PubMed
13. Feng L, Wang K, Powell J, Zhou H. Controllable synthesis of metal-organic frameworks and their hierarchical assemblies. *Matter* 2019;1:801-24. DOI
14. Khan NA, Hasan Z, Jhung SH. Beyond pristine metal-organic frameworks: Preparation and application of nanostructured, nanosized, and analogous MOFs. *Coord Chem Rev* 2018;376:20-45. DOI
15. Chen L, Luque R, Li Y. Controllable design of tunable nanostructures inside metal-organic frameworks. *Chem Soc Rev* 2017;46:4614-30. DOI PubMed
16. Shen Y, Pan T, Wang L, Ren Z, Zhang W, Huo F. Programmable logic in metal-organic frameworks for catalysis. *Adv Mater* 2021;33:e2007442. DOI PubMed
17. Guan BY, Yu XY, Wu HB, Lou XWD. Complex nanostructures from materials based on metal-organic frameworks for electrochemical energy storage and conversion. *Adv Mater* 2017;29:1703614. DOI PubMed
18. Qiu LG, Xu T, Li ZQ, et al. Hierarchically micro- and mesoporous metal-organic frameworks with tunable porosity. *Angew Chem Int Ed Engl* 2008;47:9487-91. DOI PubMed
19. Li W, Liu J, Zhao D. Mesoporous materials for energy conversion and storage devices. *Nat Rev Mater* 2016;1:16023. DOI
20. Wu Z, Lv Y, Xia Y, Webley PA, Zhao D. Ordered mesoporous platinum@graphitic carbon embedded nanophase as a highly active, stable, and methanol-tolerant oxygen reduction electrocatalyst. *J Am Chem Soc* 2012;134:2236-45. DOI PubMed
21. Xu X, Zhang Z, Wang X. Well-defined metal-organic-framework hollow nanostructures for catalytic reactions involving gases. *Adv Mater* 2015;27:5365-71. DOI PubMed
22. Xu H, Han J, Zhao B, et al. A facile dual-template-directed successive assembly approach to hollow multi-shell mesoporous metal-

organic framework particles. *Nat Commun* 2023;14:8062. DOI PubMed PMC
23. Dai S, Tissot A, Serre C. Recent progresses in metal–organic frameworks based core–shell composites. *Adv Energy Mater* 2022;12:2100061. DOI
24. Feng L, Wang KY, Lv XL, Yan TH, Zhou HC. Hierarchically porous metal-organic frameworks: synthetic strategies and applications. *Natl Sci Rev* 2020;7:1743-58. DOI PubMed PMC
25. He HH, Yuan JP, Cai PY, et al. Yolk-shell and hollow Zr/Ce-UiO-66 for manipulating selectivity in tandem reactions and photoreactions. *J Am Chem Soc* 2023;145:17164-75. DOI PubMed
26. Zhao S, Wang Y, Dong J, et al. Ultrathin metal–organic framework nanosheets for electrocatalytic oxygen evolution. *Nat Energy* 2016;1:16184. DOI
27. Dhakshinamoorthy A, Asiri AM, Garcia H. 2D metal-organic frameworks as multifunctional materials in heterogeneous catalysis and electro/photocatalysis. *Adv Mater* 2019;31:e1900617. DOI PubMed
28. He T, Ni B, Zhang S, et al. Ultrathin 2D zirconium metal-organic framework nanosheets: preparation and application in photocatalysis. *Small* 2018;14:e1703929. DOI PubMed
29. Liu W, Yin R, Xu X, Zhang L, Shi W, Cao X. Structural engineering of low-dimensional metal-organic frameworks: synthesis, properties, and applications. *Adv Sci* 2019;6:1802373. DOI PubMed PMC
30. Saad A, Biswas S, Gkaniatsou E, et al. Metal–organic framework based 1D nanostructures and their superstructures: synthesis, microstructure, and properties. *Chem Mater* 2021;33:5825-49. DOI
31. Wang J, Feng T, Chen J, He JH, Fang X. Flexible 2D Cu metal: organic framework@MXene film electrode with excellent durability for highly selective electrocatalytic $NH_3$ synthesis. *Research* 2022;2022:9837012. DOI PubMed PMC
32. Han J, Xu H, Zhao B, et al. "Hard" emulsion-induced interface super-assembly: a general strategy for two-dimensional hierarchically porous metal–organic framework nanoarchitectures. *J Am Chem Soc* 2024;146:18979-88. DOI
33. Furukawa S, Hirai K, Nakagawa K, et al. Heterogeneously hybridized porous coordination polymer crystals: fabrication of heterometallic core-shell single crystals with an in-plane rotational epitaxial relationship. *Angew Chem Int Ed Engl* 2009;48:1766-70. DOI PubMed
34. Li T, Sullivan JE, Rosi NL. Design and preparation of a core-shell metal-organic framework for selective $CO_2$ capture. *J Am Chem Soc* 2013;135:9984-7. DOI PubMed
35. Haldar R, Wöll C. Hierarchical assemblies of molecular frameworks - MOF-on-MOF epitaxial heterostructures. *Nano Res* 2021;14:355-68. DOI
36. Chai H, Yu K, Zhao Y, et al. MOF-On-MOF dual enzyme-mimic nanozyme with enhanced cascade catalysis for colorimetric/chemiluminescent dual-mode aptasensing. *Anal Chem* 2023;95:10785-94. DOI PubMed
37. Qin Y, Li Z, Duan Y, Guo J, Zhao M, Tang Z. Nanostructural engineering of metal-organic frameworks: construction strategies and catalytic applications. *Matter* 2022;5:3260-310. DOI
38. Zhao M, Huang Y, Peng Y, Huang Z, Ma Q, Zhang H. Two-dimensional metal-organic framework nanosheets: synthesis and applications. *Chem Soc Rev* 2018;47:6267-95. DOI PubMed
39. Cirujano FG, Martin N, Wee LH. Design of hierarchical architectures in metal–oganic frameworks for catalysis and adsorption. *Chem Mater* 2020;32:10268-95. DOI
40. Qiao J, Liu X, Zhang L, Liu Y. Self-assembly of 3p-block metal-based metal-organic frameworks from structural perspective. *Chem Res Chin Univ* 2022;38:31-44. DOI
41. Zhang J, Shen Y, Jin N, et al. Chemo-biocascade reactions enabled by metal-organic framework micro-nanoreactor. *Research* 2022;2022:9847698. DOI PubMed PMC
42. Xu X, Deng Q, Chen HC, et al. Metal-organic frameworks offering tunable binary active sites toward highly efficient urea oxidation electrolysis. *Research* 2022;2022:9837109. DOI PubMed PMC
43. Zheng HQ, Zhang L, Lu M, et al. Precise design and deliberate tuning of turn-on fluorescence in tetraphenylpyrazine-based metal-organic frameworks. *Research* 2022;2022:9869510. DOI PubMed PMC
44. Li K, Yang J, Gu J. Hierarchically porous MOFs synthesized by soft-template strategies. *Acc Chem Res* 2022;55:2235-47. DOI PubMed
45. Shen K, Zhang L, Chen X, et al. Ordered macro-microporous metal-organic framework single crystals. *Science* 2018;359:206-10. DOI PubMed
46. Wei Y, Zou L, Wang H, Wang Y, Xu Q. Micro/nano-scaled metal-organic frameworks and their derivatives for energy applications. *Adv Energy Mater* 2022;12:2003970. DOI
47. Han X, Zhang T, Wang X, et al. Hollow mesoporous atomically dispersed metal-nitrogen-carbon catalysts with enhanced diffusion for catalysis involving larger molecules. *Nat Commun* 2022;13:2900. DOI PubMed PMC
48. Zhou X, Jin H, Xia BY, Davey K, Zheng Y, Qiao SZ. Molecular cleavage of metal-organic frameworks and application to energy storage and conversion. *Adv Mater* 2021;33:e2104341. DOI PubMed
49. Li K, Yang J, Huang R, Lin S, Gu J. Ordered large-pore mesoMOFs based on synergistic effects of triblock polymer and hofmeister ion. *Angew Chem Int Ed Engl* 2020;59:14124-8. DOI PubMed
50. Li C, Li Q, Kaneti YV, Hou D, Yamauchi Y, Mai Y. Self-assembly of block copolymers towards mesoporous materials for energy storage and conversion systems. *Chem Soc Rev* 2020;49:4681-736. DOI PubMed
51. Liu M, Hudson ZM. Macro-/mesoporous metal–organic frameworks templated by amphiphilic block copolymers enable enhanced

uptake of large molecules. *Adv Funct Mater* 2023;33:2214262. DOI

52. Chen J, Li K, Yang J, Gu J. Hierarchical large-pore MOFs templated from poly(ethylene oxide)-*b*-polystyrene diblock copolymer with tuneable pore sizes. *Chem Commun* 2022;58:10028-31. DOI PubMed
53. You Y, Li F, Ai Y, et al. Diblock copolymers directing construction of hierarchically porous metal-organic frameworks for enhanced-performance supercapacitors. *Nanotechnology* 2021;32:165601. DOI PubMed
54. Yang J, Li K, Gu J. Hierarchically macro-microporous Ce-based MOFs for the cleavage of DNA. *ACS Mater Lett* 2022;4:385-91. DOI
55. Li K, Lin S, Li Y, Zhuang Q, Gu J. Aqueous-phase synthesis of mesoporous Zr-based MOFs templated by amphoteric surfactants. *Angew Chem Int Ed Engl* 2018;57:3439-43. DOI PubMed
56. Li K, Zhao Y, Yang J, Gu J. Nanoemulsion-directed growth of MOFs with versatile architectures for the heterogeneous regeneration of coenzymes. *Nat Commun* 2022;13:1879. DOI PubMed PMC
57. Wu T, Chen G, Han J, et al. Construction of three-dimensional dendritic hierarchically porous metal-organic framework nanoarchitectures via noncentrosymmetric pore-induced anisotropic assembly. *J Am Chem Soc* 2023;145:16498-507. DOI PubMed
58. Wang C, Zhang H, Wang Y, et al. A general strategy for the synthesis of hierarchically ordered metal-organic frameworks with tunable macro-, meso-, and micro-pores. *Small* 2023;19:e2206116. DOI PubMed
59. Yang Q, Yang CC, Lin CH, Jiang HL. Metal-organic-framework-derived hollow N-doped porous carbon with ultrahigh concentrations of single Zn atoms for efficient carbon dioxide conversion. *Angew Chem Int Ed Engl* 2019;58:3511-5. DOI PubMed
60. Li C, Pan Y, Xiao T, et al. Metal organic framework cubosomes. *Angew Chem Int Ed Engl* 2023;62:e202215985. DOI PubMed
61. Li Q, Dai Z, Wu J, et al. Fabrication of ordered macro-microporous single-crystalline MOF and its derivative carbon material for supercapacitor. *Adv Energy Mater* 2020;10:1903750. DOI
62. Hong H, Liu J, Huang H, et al. Ordered macro-microporous metal-organic framework single crystals and their derivatives for rechargeable aluminum-ion batteries. *J Am Chem Soc* 2019;141:14764-71. DOI PubMed
63. Song Y, Song X, Wang X, et al. Two-dimensional metal-organic framework superstructures from ice-templated self-assembly. *J Am Chem Soc* 2022;144:17457-67. DOI PubMed
64. Li Z, Xing X, Meng D, et al. Hierarchical structure with highly ordered macroporous-mesoporous metal-organic frameworks as dual function for $CO_2$ fixation. *iScience* 2019;15:514-23. DOI PubMed PMC
65. Li K, Yang J, Li C, Gu J. Trimodal hierarchical porous metal–organic frameworks with tunable mesoporous core–shell architectures. *ACS Mater Lett* 2024;6:233-9. DOI
66. Zhao T, Wang X, Sun Z, et al. Hollow mesoporous metal organic framework single crystals enabled by growth kinetics control for enhanced photocatalysis. *Adv Funct Mater* 2023;33:2303644. DOI
67. Liu C, Sun Q, Lin L, et al. Ternary MOF-on-MOF heterostructures with controllable architectural and compositional complexity via multiple selective assembly. *Nat Commun* 2020;11:4971. DOI PubMed PMC
68. Li Y, Di Z, Gao J, et al. Heterodimers made of upconversion nanoparticles and metal-organic frameworks. *J Am Chem Soc* 2017;139:13804-10. DOI PubMed
69. Liang J, Kou H, Ding S. Complex hollow bowl-like nanostructures: synthesis, application, and perspective. *Adv Funct Mater* 2021;31:2007801. DOI
70. Zhong G, Chen G, Han J, et al. Anisotropic interface successive assembly for bowl-shaped metal-organic framework nanoreactors with precisely controllable meso-/microporous nanodomains. *ACS Nano* 2023;17:25061-9. DOI PubMed
71. Lee G, Lee S, Oh S, Kim D, Oh M. Tip-to-middle anisotropic MOF-On-MOF growth with a structural adjustment. *J Am Chem Soc* 2020;142:3042-9. DOI PubMed
72. Zhang Q, Yang Z, Chen B, Liang X. Phase-competition-driven formation of hierarchical FeNiZn-MIL-88B-on-MOF-5 octapods displaying high selectivity for the RWGS reaction. *Chem Commun* 2019;55:8450-3. DOI PubMed
73. Kwon O, Kim JY, Park S, et al. Computer-aided discovery of connected metal-organic frameworks. *Nat Commun* 2019;10:3620. DOI PubMed PMC
74. Wang F, Fan Y, Ma Y, Li T. Sequential oriented growth of Zr-fcu-MOFs on different crystal facets of MIL-96(Al). *Cryst Growth Des* 2021;21:4571-8. DOI
75. Yu Y, Li S, Huang L, et al. Solar-driven $CO_2$ conversion promoted by MOF-on-MOF homophase junction. *Catal Commun* 2021;150:106270. DOI
76. Ren S, Duan X, Ge F, Zhang M, Zheng H. Trimetal-based N-doped carbon nanotubes arrays on Ni foams as self-supported electrodes for hydrogen/oxygen evolution reactions and water splitting. *J Power Sources* 2020;480:228866. DOI
77. Zha Q, Yuan F, Qin G, Ni Y. Cobalt-based MOF-on-MOF two-dimensional heterojunction nanostructures for enhanced oxygen evolution reaction electrocatalytic activity. *Inorg Chem* 2020;59:1295-305. DOI PubMed
78. Zhao M, Chen J, Chen B, et al. Selective epitaxial growth of oriented hierarchical metal-organic framework heterostructures. *J Am Chem Soc* 2020;142:8953-61. DOI PubMed
79. Wang XG, Xu L, Li MJ, Zhang XZ. Construction of flexible-on-rigid hybrid-phase metal-organic frameworks for controllable multi-drug delivery. *Angew Chem Int Ed Engl* 2020;59:18078-86. DOI PubMed
80. Lyu D, Xu W, Wang Y. Low-symmetry MOF-based patchy colloids and their precise linking via site-selective liquid bridging to form supra-colloidal and supra-framework architectures. *Angew Chem Int Ed Engl* 2022;61:e202115076. DOI PubMed
81. Li A, Qiao X, Liu K, Bai W, Wang T. Hollow metal organic framework improves the sensitivity and anti-interference of the detection

of exhaled volatile organic compounds. *Adv Funct Mater* 2022;32:2202805. DOI

82. Yao W, Hu A, Ding J, et al. Hierarchically ordered macro-mesoporous electrocatalyst with hydrophilic surface for efficient oxygen reduction reaction. *Adv Mater* 2023;35:e2301894. DOI PubMed
83. Cai ZX, Wang ZL, Xia YJ, et al. Tailored catalytic nanoframes from metal-organic frameworks by anisotropic surface modification and etching for the hydrogen evolution reaction. *Angew Chem Int Ed Engl* 2021;60:4747-55. DOI PubMed
84. Liu W, Huang J, Yang Q, et al. Multi-shelled hollow metal-organic frameworks. *Angew Chem Int Ed Engl* 2017;56:5512-6. DOI PubMed
85. Qin Y, Han X, Li Y, et al. Hollow mesoporous metal–organic frameworks with enhanced diffusion for highly efficient catalysis. *ACS Catal* 2020;10:5973-8. DOI
86. Liu XY, Zhang F, Goh TW, et al. Using a multi-shelled hollow metal-organic framework as a host to switch the guest-to-host and guest-to-guest interactions. *Angew Chem Int Ed Engl* 2018;57:2110-4. DOI PubMed
87. Dissegna S, Epp K, Heinz WR, Kieslich G, Fischer RA. Defective metal-organic frameworks. *Adv Mater* 2018;30:e1704501. DOI PubMed
88. Park J, Feng D, Zhou HC. Structure-assisted functional anchor implantation in robust metal-organic frameworks with ultralarge pores. *J Am Chem Soc* 2015;137:1663-72. DOI PubMed
89. Zhou Y, Yan P, Zhang S, et al. $CO_2$ coordination-driven top-down synthesis of a 2D non-layered metal–organic framework. *Fundam Res* 2022;2:674-81. DOI
90. Cai G, Ma X, Kassymova M, Sun K, Ding M, Jiang HL. Large-scale production of hierarchically porous metal-organic frameworks by a reflux-assisted post-synthetic ligand substitution strategy. *ACS Cent Sci* 2021;7:1434-40. DOI PubMed PMC
91. Huang C, Sun W, Jin Y, et al. A general synthesis of nanostructured conductive metal-organic frameworks from insulating MOF precursors for supercapacitors and chemiresistive sensors. *Angew Chem Int Ed Engl* 2024;63:e202313591. DOI PubMed
92. Yu D, Shao Q, Song Q, et al. A solvent-assisted ligand exchange approach enables metal-organic frameworks with diverse and complex architectures. *Nat Commun* 2020;11:927. DOI PubMed PMC
93. León-Alcaide L, López-Cabrelles J, Esteve-Rochina M, et al. Implementing mesoporosity in zeolitic imidazolate frameworks through clip-off chemistry in heterometallic iron-zinc ZIF-8. *J Am Chem Soc* 2023;145:23249-56. DOI PubMed PMC
94. Albolkany MK, Liu C, Wang Y, et al. Molecular surgery at microporous MOF for mesopore generation and renovation. *Angew Chem Int Ed Engl* 2021;60:14601-8. DOI PubMed
95. Bai W, Chen J, Wang X, Zhu J, Fu Y. Transformation of ZIF-67 nanocubes to ZIF-L nanoframes. *J Am Chem Soc* 2024;146:79-83. DOI PubMed
96. Dutta S, Gurumoorthi A, Lee S, et al. Sculpting in-plane fractal porous patterns in two-dimensional MOF nanocrystals for photoelectrocatalytic $CO_2$ reduction. *Angew Chem Int Ed Engl* 2023;62:e202303890. DOI PubMed
97. Wei J, Cheng N, Liang Z, et al. Heterometallic metal–organic framework nanocages of high crystallinity: an elongated channel structure formed *in situ* through metal-ion (M = W or Mo) doping. *J Mater Chem A* 2018;6:23336-44. DOI
98. Tu M, Xia B, Kravchenko DE, et al. Direct X-ray and electron-beam lithography of halogenated zeolitic imidazolate frameworks. *Nat Mater* 2021;20:93-9. DOI PubMed
99. Ai Z, Jiao L, Wang J, Jiang H. Generation of hierarchical pores in metal–organic frameworks by introducing rigid modulator. *CCS Chem* 2022;4:3705-14. DOI
100. Wang KY, Yang Z, Zhang J, et al. Creating hierarchical pores in metal-organic frameworks via postsynthetic reactions. *Nat Protoc* 2023;18:604-25. DOI PubMed
101. Zheng F, Lin T, Wang K, Wang Y, Li G. Recent advances in bimetallic metal-organic frameworks and their derivatives for thermal catalysis. *Nano Res* 2023;16:12919-35. DOI
102. Choe K, Zheng F, Wang H, et al. Fast and selective semihydrogenation of alkynes by palladium nanoparticles sandwiched in metal-organic frameworks. *Angew Chem Int Ed Engl* 2020;59:3650-7. DOI PubMed
103. Wei RJ, You PY, Duan H, et al. Ultrathin metal-organic framework nanosheets exhibiting exceptional catalytic activity. *J Am Chem Soc* 2022;144:17487-95. DOI PubMed
104. Wang Z, Ge L, Zhang G, et al. The controllable synthesis of urchin-shaped hierarchical superstructure MOFs with high catalytic activity and stability. *Chem Commun* 2021;57:8758-61. DOI PubMed
105. Xuan W, Zhu C, Liu Y, Cui Y. Mesoporous metal-organic framework materials. *Chem Soc Rev* 2012;41:1677-95. DOI PubMed
106. Cao L, Lin Z, Peng F, et al. Self-supporting metal-organic layers as single-site solid catalysts. *Angew Chem Int Ed Engl* 2016;55:4962-6. DOI PubMed
107. Zhang F, Zhang J, Zhang B, et al. $CO_2$ controls the oriented growth of metal-organic framework with highly accessible active sites. *Nat Commun* 2020;11:1431. DOI PubMed PMC
108. Chang GG, Ma XC, Zhang YX, et al. Construction of hierarchical metal-organic frameworks by competitive coordination strategy for highly efficient $CO_2$ conversion. *Adv Mater* 2019;31:e1904969. DOI PubMed
109. Cai G, Jiang HL. A modulator-induced defect-formation strategy to hierarchically porous metal-organic frameworks with high stability. *Angew Chem Int Ed Engl* 2017;56:563-7. DOI PubMed
110. Xu Z, Li L, Chen X, Fang C, Xiao G. Mesoporous zeolitic imidazolate frameworks. *CCS Chem* 2022;4:2906-13. DOI
111. Guo J, Qin Y, Zhu Y, et al. Metal-organic frameworks as catalytic selectivity regulators for organic transformations. *Chem Soc Rev* 2021;50:5366-96. DOI PubMed

112. Dunn B, Kamath H, Tarascon JM. Electrical energy storage for the grid: a battery of choices. *Science* 2011;334:928-35. DOI PubMed
113. Simon P, Gogotsi Y. Materials for electrochemical capacitors. *Nat Mater* 2008;7:845-54. DOI PubMed
114. Xu Y, Kraft M, Xu R. Metal-free carbonaceous electrocatalysts and photocatalysts for water splitting. *Chem Soc Rev* 2016;45:3039-52. DOI PubMed
115. Wachsman ED, Lee KT. Lowering the temperature of solid oxide fuel cells. *Science* 2011;334:935-9. DOI PubMed
116. Wang Y, Wang X, She P, Guan D, Song L, Xu J. Nature-inspired three-dimensional Au/spinach as a binder-free and self-standing cathode for high-performance Li-$O_2$ batteries. *Chem Res Chin Univ* 2022;38:200-8. DOI
117. Peng Y, Sanati S, Morsali A, García H. Metal-organic frameworks as electrocatalysts. *Angew Chem Int Ed Engl* 2023;62:e202214707. DOI PubMed
118. Pan X, Zhu Q, Yu K, et al. One-dimensional metal-organic frameworks: synthesis, structure and application in electrocatalysis. *Next Mater* 2023;1:100010. DOI
119. Ge K, Sun S, Zhao Y, et al. Facile synthesis of two-dimensional iron/cobalt metal-organic framework for efficient oxygen evolution electrocatalysis. *Angew Chem Int Ed Engl* 2021;60:12097-102. DOI PubMed
120. Choi WH, Moon BC, Park DG, et al. Autogenous production and stabilization of highly loaded sub-nanometric particles within multishell hollow metal-organic frameworks and their utilization for high performance in Li-$O_2$ batteries. *Adv Sci* 2020;7:2000283. DOI PubMed PMC
121. Shinde SS, Lee CH, Jung J, et al. Unveiling dual-linkage 3D hexaiminobenzene metal–organic frameworks towards long-lasting advanced reversible Zn–air batteries. *Energy Environ Sci* 2019;12:727-38. DOI
122. Meng X, Liu L, Ouyang S, et al. Nanometals for solar-to-chemical energy conversion: from semiconductor-based photocatalysis to plasmon-mediated photocatalysis and photo-thermocatalysis. *Adv Mater* 2016;28:6781-803. DOI PubMed
123. Li R, Zhang W, Zhou K. Metal-organic-framework-based catalysts for photoreduction of $CO_2$. *Adv Mater* 2018;30:e1705512. DOI PubMed
124. Li X, Yang X, Xue H, Pang H, Xu Q. Metal–organic frameworks as a platform for clean energy applications. *EnergyChem* 2020;2:100027. DOI
125. Zhan W, Sun L, Han X. Recent progress on engineering highly efficient porous semiconductor photocatalysts derived from metal-organic frameworks. *Nanomicro Lett* 2019;11:1. DOI PubMed PMC
126. Qian Y, Zhang F, Pang H. A review of MOFs and their composites-based photocatalysts: synthesis and applications. *Adv Funct Mater* 2021;31:2104231. DOI
127. Yu F, Jing X, Wang Y, Sun M, Duan C. Hierarchically porous metal-organic framework/$MoS_2$ interface for selective photocatalytic conversion of $CO_2$ with $H_2O$ into $CH_3COOH$. *Angew Chem Int Ed Engl* 2021;60:24849-53. DOI PubMed
128. Wu T, Shi Y, Wang Z, et al. Unsaturated $Ni^{II}$ centers mediated the coordination activation of benzylamine for enhancing photocatalytic activity over ultrathin Ni MOF-74 nanosheets. *ACS Appl Mater Interfaces* 2021;13:61286-95. DOI PubMed
129. He T, Chen S, Ni B, et al. Zirconium-porphyrin-based metal-organic framework hollow nanotubes for immobilization of noble-metal single atoms. *Angew Chem Int Ed Engl* 2018;57:3493-8. DOI PubMed
130. Li H, Sun Y, Yuan ZY, Zhu YP, Ma TY. Titanium phosphonate based metal-organic frameworks with hierarchical porosity for enhanced photocatalytic hydrogen evolution. *Angew Chem Int Ed Engl* 2018;57:3222-7. DOI PubMed
131. Qi SC, Sun Z, Yang ZH, et al. Photo-responsive carbon capture over metalloporphyrin-$C_{60}$ metal-organic frameworks via charge-transfer. *Research* 2023;6:0261. DOI PubMed PMC
132. Cheng X, Dao X, Wang S, Zhao J, Sun W. Enhanced photocatalytic $CO_2$ reduction activity over $NH_2$-MIL-125(Ti) by facet regulation. *ACS Catal* 2021;11:650-8. DOI
133. Guo F, Yang M, Li R, He Z, Wang Y, Sun W. Nanosheet-engineered $NH_2$-MIL-125 with highly active facets for enhanced solar $CO_2$ reduction. *ACS Catal* 2022;12:9486-93. DOI
134. Liu Z, Chen Z, Li M, et al. Construction of single Ni atom-immobilized ZIF-8 with ordered hierarchical pore structures for selective $CO_2$ photoreduction. *ACS Catal* 2023;13:6630-40. DOI
135. Liu C, Lin L, Sun Q, et al. Site-specific growth of MOF-on-MOF heterostructures with controllable nano-architectures: beyond the combination of MOF analogues. *Chem Sci* 2020;11:3680-6. DOI PubMed PMC
136. Gong X, Gnanasekaran K, Chen Z, et al. Insights into the structure and dynamics of metal-organic frameworks via transmission electron microscopy. *J Am Chem Soc* 2020;142:17224-35. DOI PubMed
137. Wang Y, Jiang ZJ, Wang DR, Lu W, Li D. Machine learning-assisted discovery of propane-selective metal-organic frameworks. *J Am Chem Soc* 2024;146:6955-61. DOI PubMed
138. Pétuya R, Durdy S, Antypov D, et al. Machine-learning prediction of metal-organic framework guest accessibility from linker and metal chemistry. *Angew Chem Int Ed Engl* 2022;61:e202114573. DOI PubMed PMC